Title

Cell-type-specific origins of locomotor rhythmicity at different speeds in larval zebrafish

Running title

Spinal rhythmogenesis during zebrafish swimming

Authors

Moneeza A. Agha[1,2], Sandeep Kishore[1], and David L. McLean[1,2,*]

Affiliations

[1] Department of Neurobiology, Northwestern University, Evanston, IL 60201

[2] Interdisciplinary Biological Sciences Graduate Program, Northwestern University, Evanston, IL 60201

* Correspondence: david-mclean@northwestern.edu

Conflict of interest

The authors declare no conflict of interest.

Acknowledgements

We are extremely grateful to Katelyn Young for technical support. Financial support provided by NIH R21 NS125187 and NIH R21 NS125207.

Abstract

Different speeds of locomotion require heterogeneous spinal populations, but a common mode of rhythm generation is presumed to exist. Here, we explore the cellular versus synaptic origins of spinal rhythmicity at different speeds by performing electrophysiological recordings from premotor excitatory interneurons in larval zebrafish. Chx10-labeled V2a neurons are divided into at least two morphological subtypes proposed to play distinct roles in timing and intensity control. Consistent with distinct rhythm generating and output patterning functions within the spinal V2a population, we find that descending subtypes are recruited exclusively at slow or fast speeds and exhibit intrinsic cellular properties suitable for rhythmogenesis at those speeds, while bifurcating subtypes are recruited more reliably at all speeds and lack appropriate rhythmogenic cellular properties. Unexpectedly, however, phasic firing patterns during locomotion in rhythmogenic and non-rhythmogenic V2a neurons alike are best explained by distinct modes of synaptic inhibition linked to cell-type and speed. At fast speeds reciprocal inhibition in descending V2a neurons supports phasic firing, while recurrent inhibition in bifurcating V2a neurons helps pattern motor output. In contrast, at slow speeds recurrent inhibition in descending V2a neurons supports phasic firing, while bifurcating V2a neurons rely on reciprocal inhibition alone to pattern output. Our findings suggest cell-type-specific, not common, modes of rhythmogenesis generate and coordinate different speeds of locomotion.

Introduction

All forms of vertebrate locomotion rely on rhythmic activity in muscles operating as functional antagonists (Grillner, 1985). For instance, swimming in fishes relies on left-right alternation of axial muscles across the body, while walking in mammals relies on flexor-extensor alternation along it. A landmark hypothesis posed over a century ago argued for corresponding excitatory 'half-centers' within spinal cord (e.g., left-right or flexor-extensor), with reciprocal, feedforward inhibition between half-centers generating rhythmic output (Brown, 1911). Since then reciprocal inhibition has been relegated to patterning activity between so-called 'unit burst generators' capable of rhythmogenesis via recurrent, feedback excitatory connections (Grillner and Kozlov, 2021).

The idea of solitary unit burst generators reliant on recurrent connectivity disconnects rhythmogenesis from activity in other unit burst generators, which helps explain the flexible patterns of coordination necessary to effectively navigate through unpredictable environments. For example, simulations adjusting the synaptic coupling strength between segmental axial unit burst generators can explain changes in the speed and direction of swimming in lampreys (Kozlov et al., 2009). Likewise, simulations altering the synaptic coupling between segmental limb unit burst generators can replicate different speeds and gaits of locomotion in cats (Grillner, 1981).

Another theory explaining speed-dependent changes in coordination stratifies 'rhythm' and 'pattern' control (Perret and Cabelguen, 1980; Koshland and Smith, 1989; Kriellaars et al., 1994; Burke et al., 2001; Lafreniere-Roula and McCrea, 2005), where populations of interneurons generating higher or lower frequency rhythms feed into separate populations coordinating distinct patterns of motor output (McCrea and Rybak, 2008; Ausborn et al., 2019). In support, studies in zebrafish and mice suggest separate spinal populations are active at different locomotor speeds with distinct patterns of motor output (McLean et al., 2008; Talpalar et al., 2013; Satou et al., 2020; Picton et al., 2022). Critically, however, rhythmogenesis is presumed to originate from a common mechanism regardless of speed, reliant on cellular properties or synaptic drive or both (Guertin, 2009; Brocard et al., 2010; Ryczko et al., 2010; Ziskind-Conhaim and Hochman, 2017; El Manira, 2023).

Here, we have explored the origins of spinal rhythmogenesis at different speeds using the larval zebrafish model system, where it is possible to link the identity, physiology and connectivity of interneurons to their recruitment patterns at different speeds of locomotion. Like all fish, larval zebrafish generate two basic modes of forward swimming or 'gaits' (Di Santo et al., 2021). Anguilliform mode is typically reserved for escaping predators and uses higher frequency/amplitude oscillations of the trunk, while carangiform mode utilizes lower frequency/amplitude oscillations of the tail for exploration and pursuing prey (Budick and O'Malley, 2000; Muller and van Leeuwen, 2004; Thorsen et al., 2004; Patterson et al., 2013; Bhattacharyya et al., 2021).

Swimming at different speeds is generated by axial motor neurons organized into fast, slow and intermediate units distinguished by birth order (Myers et al., 1986), size (McLean et al., 2007), relative

innervation of fast and slow muscle fibers (Bello-Rojas et al., 2019), and molecular signatures (D'Elia et al., 2023; Pallucchi et al., 2024). Current-clamp and voltage-clamp recordings from motor neurons have revealed differences in rhythmogenic cellular properties and synaptic drive between the different types (Menelaou and McLean, 2012; Kishore et al., 2014), suggesting different forms of rhythmogenesis could be responsible for different speeds of locomotion. To test this idea, we performed current-clamp and voltage-clamp recordings from Chx10-labeled spinal V2a interneurons, which provide a major source of phasic premotor excitation during locomotion in zebrafish and mice (McLean and Dougherty, 2015).

We find that morphologically distinct V2a neurons sort into rhythm-generating and pattern-forming subtypes based on distinct cellular properties linked to distinct patterns of recruitment and synaptic drive. Critically, among descending V2a neurons that qualify as rhythm-generating, reciprocal inhibition originating from contralateral sources supports phasic firing patterns at fast speeds, while recurrent inhibition from ipsilateral sources supports phasic firing patterns at slow speeds. For bifurcating V2a neurons considered pattern-forming, the opposite is true – recurrent inhibition supports phasic firing at fast speeds and reciprocal inhibition at slow speeds. Ultimately, our findings reveal unexpected cell-type-specific and speed-dependent complexity in the mechanisms of spinal rhythmogenesis underlying locomotion.

Results

Identifying V2a neurons for recordings during 'fictive' escape swimming

From our previous work studying V2a neurons in larval zebrafish we know they are organized into: 1) fast and slow subtypes based on dorso-ventral soma position and birth order (McLean et al., 2007; McLean et al., 2008; McLean and Fetcho, 2009), and 2) distinct subtypes that provide stronger direct versus indirect control of motor neuron recruitment (Menelaou et al., 2014; Menelaou and McLean, 2019). Specifically, V2a neurons with descending axons (V2a-D) provide stronger inputs to other premotor interneurons, while V2a neurons with bifurcating axons (V2a-B) provide stronger inputs to motor neurons (Menelaou and McLean, 2019), in line with differential rhythm and pattern control. However, we do not know if the same mechanisms of rhythmogenesis shape the phasic activation of distinct V2a types at different speeds.

To record from distinct types of V2a neurons, we targeted GFP-positive neurons located at midbody in the Tg(Chx10:GFP) line (Fig. 1A,B)(Kimura et al., 2006), since midbody neurons would be recruited during both fast anguilliform and slow carangiform modes (Muller and van Leeuwen, 2004; Thorsen et al., 2004). V2a-D and V2a-B neurons recruited at fast speeds can be distinguished by levels of Chx10 expression in transgenic lines (Menelaou and McLean, 2019), as reported in mice (Hayashi et al., 2018). To get a better sense of differences in the number and spatial distribution of distinct types, we split GFP-positive neurons into two categories based on a bimodal distribution of fluorescence intensity and normalized their soma positions to dorso-ventral and medio-lateral axes in the spinal cord. Larger, dimmer V2a neurons intermingled with smaller, brighter neurons along the dorso-ventral axis (Fig. 1C, *left*), but occupied more lateral positions (Fig. 1C, *right*). Statistical analysis confirmed these observations,

with no significant difference in either dorso-ventral distribution (Fig. 1D, *left*) or number per segment between the low or high GFP-positive types (Fig. 1D, *right*), but a significant difference in mediolateral position (Fig. 1E).

To evaluate firing patterns and synaptic drive responsible for rhythmogenesis in different types, we recorded from V2a neurons during 'fictive' swimming evoked by a mild electrical shock, while simultaneously monitoring rhythmic motor output using ventral rootlet recordings (Fig. 1F). During real swimming escape responses decelerate (Video 1), beginning in fast anguilliform mode and ending in slow carangiform mode (McLean et al., 2008; McLean and Fetcho, 2009). Plots of ventral rootlet burst frequencies with time confirm this pattern during 'fictive' escape responses, where we observe the highest frequencies at the beginning of the swim episode immediately following the stimulus (Fig. 1G, *left*). Notably, zebrafish swimming is episodic (McHenry and Lauder, 2006; Soto and McHenry, 2020) and so it can continue intermittently after the initial escape swim episode. Subsequent episodes (Swim 2+) rarely exceeded peak firing frequencies observed in the first stimulus-evoked episode (> 60 Hz in swim 1) and there was more variability in frequency (Fig. 1G, *right*). For purposes of analysis we pooled data from the first (Swim 1) and subsequent (Swim 2+) episodes to capture as broad a frequency range as possible.

Thus, V2a neurons can be easily distinguished for targeting purposes using levels of GFP expression and we can assess their firing and synaptic drive during fast anguilliform and slow carangiform modes distinguished by frequency and temporal sequence within fictive escape swim episodes. This set the stage for asking if the same mechanism of rhythmogenesis drives the phasic activation of distinct V2a types at different speeds.

Differences in intrinsic rhythmogenesis related to V2a neuron type

Rhythmogenesis can originate from cellular properties or synaptic drive or some combination of the two (Marder and Calabrese, 1996; Marder and Bucher, 2001). In theory, neurons that are intrinsically rhythmogenic can create patterned outputs from unpatterned inputs. Thus, to explore the intrinsic rhythmicity of V2a neurons we performed whole-cell current-clamp recordings from high and low GFP-positive V2a neurons and tested their firing responses to stable current steps. By including dye in our recording pipette, we confirmed post-hoc that all high GFP neurons we targeted for recordings were V2a-Ds and all low GFP neurons were V2a-Bs (Fig. 2A), as we would expect based on our prior work (Menelaou and McLean, 2019). Differences in sizes and dorso-ventral distributions of V2a-D and V2a-B neurons in our current-clamp dataset (n = 47) were consistent with our analysis of high and low GFP neurons in stable lines (Fig. 2B, *left*). Also, measurements of input resistance and rheobase current were consistent with differences in sizes and excitability between the two types (Fig. 2C, *left*). Thus, we were confident of a sufficient sampling of V2a neurons to explore differences in rhythmogenic capacity related to type and recruitment order.

V2a-D neurons with 'tonic' responses and V2a-B neurons with higher frequency 'chattering' ones were distributed dorsally and had the lowest input resistances in their respective types (Fig. 2B-E). In tonic

V2a-Ds, firing above rheobase current was observed consistently throughout the current step (Fig. 2E, *top*), with instantaneous spike rates increasing linearly with increasing current, starting around 40 Hz and reaching 200 Hz (Fig. 2D). In chattering V2a-Bs, firing above rheobase current was intermittent throughout the step (Fig. 2F, *top*), with instantaneous rates starting around 200 Hz and reaching 600 Hz (Fig. 2D). These observations are consistent with previous recordings from fast V2a-D and V2a-B neurons (Menelaou and McLean, 2019).

On the other hand, V2a-D and V2a-B neurons with 'burst' responses were distributed ventrally and had the highest input resistances within their respective types (Fig. 2B-E). In bursting V2a neurons, firing above rheobase was characterized by higher frequency spikes superimposed on lower frequency membrane potential oscillations (Fig. 2E-F, *bottom*). While the frequency of the slower oscillations increased with current (Fig. 2E-F, *bottom*), instantaneous spike rates were already close to peak values at rheobase (500-600 Hz; Fig. 2D). Beyond 2-3x rheobase current, slower oscillations were no longer obvious and the firing pattern more closely resembled the chattering one (data not shown), as observed previously for motor neurons (Menelaou and McLean, 2012).

Next, we compared the firing properties of distinct types of V2a neurons to their recruitment patterns during fictive escape swimming. As expected (Menelaou and McLean, 2019), both tonic V2a-D and chattering V2a-B neurons were recruited at the beginning of the episode at median swim frequencies above 30 Hz (Fig. 2G-H), consistent with recruitment during fast anguilliform mode (Thorsen et al., 2004; McLean et al., 2008; McLean and Fetcho, 2009). In contrast, burst V2a-Ds fired more reliably at the end of the episode at median frequencies that rarely exceeded 30 Hz (Fig. 2G-H), consistent with participation in slow carangiform mode (Thorsen et al., 2004; McLean et al., 2008; McLean and Fetcho, 2009). Burst V2a-Bs were recruited just below 30 Hz, and fired more reliably throughout the episode and over a broader frequency range (Fig. 2G-H), particularly compared to the narrow range of bursting V2a-Ds (two sample Kolmogrov-Smirnov test on density distributions; $D = 0.157$, $p < 0.001$; BB, $n = 6$, BD, $n = 8$). A comparison between the step firing and swim firing patterns among V2a-D neurons revealed a remarkable correspondence (Fig. 2G), with median spike frequencies (tonic) or oscillation frequencies (burst) overlapping median recruitment frequencies during swimming (Fig. 2I, *left*). However, the link between step firing and swim firing patterns was less obvious for V2a-B neurons (Fig. 2G). For example, while bursting V2a-B neurons recruited at swim frequencies exceeding 60 Hz had higher frequency oscillations, step bursting rarely exceeded 20 Hz (Fig. 2I, *right*). For chattering V2a-B neurons, there were no clear subthreshold oscillations to calculate rhythmicity and the broad range of spike frequencies resulted in large standard deviations (±74–130 Hz, $n = 5$) that rendered median values less interpretable.

Thus, distinct electrophysiological properties define distinct V2a types recruited at different speeds and V2a-D neurons are better suited to providing intrinsic rhythmogenic activity during fast and slow swimming modes. This is consistent with their proposed rhythm-generating and pattern-forming roles

176 (Menelaou and McLean, 2019), and suggests V2a-B neurons rely more on rhythmic synaptic drive to
177 shape their phasic firing patterns during swimming.

178 *Both types of V2a neuron operate at slow and fast speeds*

179 Our current-clamp data suggest that different types would rely differently on cellular properties versus
180 synaptic drive for rhythmogenesis. To test this idea more directly, we performed voltage-clamp recordings
181 during fictive escape swimming. To more effectively isolate synaptic currents, we included cesium in the
182 patch solution. Since this blocks voltage-gated channels and spiking, we needed to classify fast and slow
183 V2a-D and V2a-B neurons subtypes by first monitoring spikes in cell-attached mode. Consistent with our
184 current-clamp recordings, in our voltage-clamp dataset (n = 39) we found V2a-D and V2a-B neurons that
185 fired at the beginning of the escape episode or nearer the end (Fig. 3A). V2a-D neurons fired more
186 sparsely (Fig. 3A, *left*) and were divided into two distinct groups: 1) neurons that fired exclusively at the
187 beginning of the episode at median swim frequencies exceeding 40 Hz, and 2) neurons that fired later on
188 in the episode at median swim frequencies rarely exceeding 30 Hz (Fig. 3B, *top and bottom left*; 3C). On
189 the other hand, V2a-B neurons fired more reliably (Fig. 3A, *right*) and median values were more
190 continuous, making it more difficult to group neurons based on location within the episode (Fig. 3B, *top*
191 *and bottom right*) or swim frequency (Fig. 3D).

192 To better segregate both types of V2a neurons based on speed, we used the frequency-dependent
193 transition between anguilliform and carangiform modes to define V2a neurons recruited more reliably
194 below 35 Hz as 'slow' and V2a neurons recruited more reliably above 35 Hz as 'fast' (Fig. 4A). Consistent
195 with our current-clamp recordings, slow V2a-D and V2a-B neurons in our voltage-clamp recordings were
196 more ventrally distributed with higher resistances than fast V2a-D and V2a-B neurons (Fig. 4B). A closer
197 examination of spike timing relative to individual ventral rootlet bursts revealed median spike
198 distributions in advance of the center of the motor burst, as expected for premotor excitatory
199 interneurons involved in rhythmogenesis (Fig. 4C). Plots of spike densities normalized to center burst
200 revealed that V2a-B neurons begin to fire slightly in advance of V2a-D neurons (Fig. 4D), consistent with
201 differences in membrane resistance related to size, where neurons with faster time constants respond
202 more quickly to synaptic inputs (Menelaou and McLean, 2019).

203 Next, to explore recruitment probability as a function of speed in more depth we divided the full range of
204 fictive swimming frequencies into four bins distributed around 35 Hz. For V2a-D neurons, fast neurons
205 were rarely recruited below 35 Hz and increased to a maximum of 50% recruitment reliability per motor
206 burst above 35 Hz (Fig. 4E, *top left*). Similarly, slow V2a-D neurons did not exceed 50% recruitment
207 reliability per motor burst below 35 Hz and rarely fired above it (Fig. 4E, *top right*). When collapsed into
208 two bins below and above 35 Hz, these differences in recruitment probability were significant (Fig. 4F,
209 *top*). For V2a-B neurons, fast neurons fired more reliably below 35Hz than fast V2a-Ds and increased to
210 100% recruitment reliability per motor burst above 35 Hz (Fig. 4E, *bottom left*). Similarly, slow V2a-B
211 neurons fired more reliably above 35 Hz than slow V2a-Ds, and at 100% reliability below it (Fig. 4E,

212 *bottom right*). Binning of recruitment among V2a-Bs revealed significant differences related to speed
213 among the fast subtypes only (Fig. 4F, *bottom*). Among the slow V2a-Bs, decreases in recruitment
214 reliability were observed in the majority of neurons (n = 5 of 6), however the difference was not significant
215 when pooled (Fig. 4F, *bottom*).

216 In further support of the speed-based modular organization of V2a neurons, in slow types higher
217 instantaneous spike rates were observed at lower burst frequencies, while in fast types higher spike rates
218 were observed at higher burst frequencies (Fig. 4G, *top*). Critically, spike rates observed during fictive
219 swimming overlap with those observed during current steps between 1-2x rheobase, ranging from in 200-
220 600 Hz (Fig. 4H, *top*), with the fastest spike rates observed in fast V2a-B neurons. This suggests that the
221 firing patterns observed during current injections between 1-2x rheobase are functionally relevant. When
222 we measured spike numbers per burst, lower numbers were consistently observed at higher burst
223 frequencies regardless of type or speed class (Fig. 4G, *bottom*) consistent with less time to spike during
224 shorter cycle periods. In addition, V2a-B neurons fired significantly more spikes per burst than V2a-Ds on
225 average (Fig. 4H, *bottom*), consistent with their higher recruitment probabilities.

226 Thus, within our voltage-clamp dataset we have V2a-D and V2a-B neurons operating during anguilliform
227 and carangiform swimming modes. While V2a-D neurons fire more sparsely and in a stricter modular
228 fashion, V2a-B neurons fire more reliably and over a broader range of frequencies, consistent with
229 occupation of a pattern forming layer downstream of distinct fast and slow rhythmic signals.

230 *Differences in the levels of synaptic drive mirror differences in speed modularity*

231 To get a better sense of the relative segregation of synaptic inputs to V2a-D and V2a-B neurons based on
232 speed, we first focused on the maximum amplitude of excitatory and inhibitory currents recorded during
233 fictive escape swimming. Clamping V2a neurons at a potential to isolate excitatory post-synaptic currents
234 (EPSCs) revealed faster time course, compound EPSCs superimposed on a slower, tonic inward current
235 (Fig. 5A,B). While tonic excitation was observed the entirety of the episode, fast V2a-Ds received
236 compound EPSCs exclusively during high frequency swimming at the beginning (Fig. 5A, *top*), while slow
237 V2a-D's received compound EPSCs exclusively during slower swimming later in the episode (Fig. 5A,
238 *bottom*), consistent with their recruitment patterns. A similar pattern was observed among V2a-Bs,
239 however compound EPSCs were observed over a broader range of frequencies (Fig. 5B), also consistent
240 with their recruitment patterns. We also noted differences in maximum levels of current related to type.
241 When we plotted maximum current (tonic current + compound EPSCs) versus input resistance, we
242 observed a significant negative correlation, with lower resistance V2a-Bs receiving orders of magnitude
243 more excitation than higher resistance V2a-Ds (Fig. 5C). This is consistent with peak excitatory drive
244 normalized to cellular excitability, as reported previously (Menelaou et al., 2022).

245 Next, clamping V2a neurons at a potential to isolate inhibitory post-synaptic currents (IPSCs) revealed
246 faster time course compound IPSCs superimposed on a slower, tonic outward current (Fig. 5D-E). In all
247 V2a types tonic inhibition persisted the entirety of the episode and compound IPSCs were larger at higher

248 frequencies near the beginning (Fig. 5D-E). Like excitation, plots of maximum current (tonic current +
249 compound IPSCs) revealed a significant negative correlation between inhibitory current and input
250 resistance (Fig. 5F), meaning that peak inhibitory drive is also normalized to cellular excitability. Given
251 these large differences in maximum current values, to compare frequency-dependent changes in
252 excitation and inhibition, we normalized the currents for each cycle to the maximum currents for the
253 neuron (Fig. 5C, 5F). So, maximum EPSCs or IPSCs in a given cycle are expressed as a percentage of the
254 maximum value in all cycles at any speed.

255 For fast V2a-D and V2a-B neurons, maximum excitatory drive increased with increasing frequency (Fig.
256 5G, *left*). Differences in maximum excitation were significant for both types when data were pooled (Fig.
257 5H), consistent with their recruitment patterns (Fig. 4F). Inhibition also followed the same pattern for
258 fast V2a neurons (Fig. 5I, *left*), significantly increasing at fast speeds (Fig. 5J). For slow V2a-D neurons
259 excitation was significantly lower at higher frequencies (Fig. 5G, *top right*; 5H, *top*) and inhibition was
260 significantly higher (Fig. 5I, *top right*; 5J, *top*). However, for slow V2a-B neurons neither excitation (Fig.
261 5G, *bottom right*; 5H, *bottom*) nor inhibition (Fig. 5I, *bottom right*; 5J, *bottom*) changed significantly
262 when pooled, despite the decreases in excitation (n = 4 of 6) and increases in inhibition (n = 5 of 6) in the
263 majority of neurons. These patterns of excitation and inhibition are consistent with recruitment patterns,
264 where slow V2a-D neurons are silenced at fast speeds and slow V2a-B neurons are recruited albeit with
265 lower reliability (Fig. 4F).

266 While the increase in inhibition at fast speeds to slow V2a neurons makes sense in terms of their
267 disengagement during fast anguilliform mode (McLean et al., 2008), the increase in inhibition to fast V2a
268 neurons clearly does not have a similar impact, despite being normalized to excitability. Indeed, when we
269 compared the maximum excitation and inhibition to V2a-Ds (Fig. 5K) and V2a-Bs (Fig. 5L), maximum
270 inhibition was orders of magnitude larger than maximum excitation. Even when controlling for
271 differences in driving forces experienced at resting potentials, it would be difficult for V2a neurons to fire
272 if excitation and inhibition arrived concurrently.

273 Thus, measurements of maximum levels of excitatory and inhibitory drive that include fast phasic and
274 slower tonic components are consistent with recruitment patterns. These data also suggest the timing of
275 inhibition plays a critical role in shaping the rhythmic output of V2a neurons more broadly.

276 *Differences in the timing of synaptic drive better explain rhythmic V2a recruitment*

277 To compare the timing of compound EPSCs and IPSCs we normalized the amplitude to the maximum (1)
278 and minimum (0) values for that cycle and normalized the timing to the phase of the swim cycle, with the
279 centers of two successive motor bursts demarcating phase 0 and 1 (Fig. 6A). To simplify comparisons
280 between peaks in excitation and troughs in inhibition, we inverted the sign of excitation. By convention,
281 synaptic currents arriving between 0.75 – 0.25 are described as 'in-phase' with local motor output, while
282 currents arriving 0.25 – 0.75 are described as 'anti-phase'. In frog tadpoles and adult lampreys, in-phase
283 currents are assumed to arise from recurrent sources on the ipsilateral side, while anti-phase currents

284 arise from the reciprocal sources on the contralateral side (Soffe and Roberts, 1982; Russell and Wallen,
285 1983). This means that differences in the timing of peaks of excitation and inhibition can be used to draw
286 inferences about patterns of connectivity along and across the body, with phase-advanced inputs from
287 more rostral regions and phase-delayed inputs from more caudal ones.

288 First, to assess differences in the timing of compound EPSCs and IPSCs, we low pass filtered the raw
289 current trace to identify peaks in-phase and anti-phase (Fig. 6A, *black dots*), which were then plotted on a
290 circular axis and compared to cell-attached spiking activity (Fig. 6B-D). For all V2a neurons, spikes were
291 exclusively distributed in-phase with local motor output (Fig. 6B), with largely overlapping distributions
292 that were broader for fast V2a-Ds (Fig. 6B, *top*) and slow V2a-Bs (Fig. 6B, *bottom*), consistent with spike
293 distributions observed in real-time (Fig. 4D). However, there were type-specific differences in the
294 distributions of peak excitation and inhibition.

295 For both fast and slow V2a-Ds phasic excitation began early in anti-phase, while the distribution of phasic
296 excitation in fast and slow V2a-Bs was more coherent and trailed that of V2a-Ds (Fig. 6C). This is
297 consistent with the proposed hierarchical organization of V2a neurons, with V2a-Ds occupying a position
298 upstream of V2a-Bs, which is not as obvious based purely on spike distributions (Fig. 4D, 6B). For fast
299 V2a-Ds, phasic inhibition was also broadly distributed, with a dip that coincided with the peak
300 distributions of both excitation and spiking activity (Fig. 6D, *top*). For slow V2a-Ds, there were two clear
301 peaks in phasic inhibition, one immediately trailing in-phase excitation (Fig. 6D, *bottom arrow*) and one
302 peaking anti-phase. Remarkably, for V2a-B neurons, we observed the opposite pattern for phasic
303 inhibition. Fast V2a-Bs received peaks in-phase and anti-phase (Fig. 6D, *top arrow*), while slow V2a-Bs
304 received predominantly anti-phase inhibition (Fig. 6D, *bottom*). Notably, the presence of in-phase
305 inhibition was also associated with a more coherent distribution of spikes in slow V2a-Ds and fast V2a-Bs
306 (c.f., Fig. 6B).

307 Next, to get a better sense of how patterns of phasic excitation and inhibition ultimately shape phasic
308 firing patterns within different types at different speeds, we binned the data by frequency as above and
309 examined averages of normalized raw current traces. Among the V2a-Ds, fast subtypes exhibited
310 reciprocal inhibition at all frequencies, with phasic peaks in excitation and inhibition most obvious at
311 higher frequencies coincident with spiking activity (Fig. 6E, *top*). Among slow V2a-Ds, coherent peaks in
312 reciprocal and recurrent inhibition were most obvious at slow speeds coincident with phasic excitation
313 and spiking behavior (Fig. 6E, *bottom*). Among the V2a-Bs, patterns of reciprocal and recurrent inhibition
314 were consistent across all speed bins, with peaks in phasic excitation and dips in phasic inhibition
315 coincident with spiking activity (Fig. 6F).

316 Thus, despite differences in cellular rhythmogenic capacity, these observations suggest all types of V2a
317 neurons rely on phasic excitation and inhibition to sculpt their rhythmic firing behavior during
318 swimming. Peaks in phasic excitation arrive earlier among V2a-D neurons consistent with their
319 hierarchical positioning upstream from V2a-B neurons, and the relative coherence of phasic excitatory

320 and inhibitory drive at different frequencies is consistent with speed modularity in this population.
321 Among V2a-B neurons, the coherence of phasic excitatory and inhibitory drive over the entire frequency
322 range is consistent with a role integrating inputs from the different speed modules. Critically, these data
323 also suggest reciprocal inhibition plays a key role in rhythmogenesis at fast speeds, while recurrent
324 inhibition plays a more dominant role in rhythmogenesis at slow speeds.

325 *Synaptic silencing of reciprocal inhibition has speed-dependent effects on rhythm versus pattern*

326 Our data thus far suggest that reciprocal inhibition plays a key role in rhythmogenesis at fast speeds via
327 V2a-D neurons, while it plays a more dominant role patterning output at slow speeds via V2a-B neurons.
328 To test this idea, we used a genetic approach to synaptically silence commissural, glycinergic Dmrt3a-
329 labeled dI6 neurons (Fig. 7A,B), which participate in swimming over a range of speeds in larvae (Kishore
330 et al., 2020; Satou et al., 2020). Specifically, we crossed compound Tg[Dmrt3a:Gal4;UAS:pTagRFP] fish
331 (Satou et al., 2013; Kishore et al., 2020) with Tg[UAS:BoTxBLC-GFP] fish (Sternberg et al., 2016), to
332 express botulinum toxin (light chain) fused with GFP (BoTx-GFP) selectively in dI6 neurons and
333 monitored the impact on locomotor rhythmogenesis using contralateral ventral rootlet recordings. As
334 controls, we performed recordings from heterozygous sibling larvae that lacked expression of BoTx-GFP.

335 First, to confirm the efficacy of synaptic silencing, we analyzed the distribution of dI6 neurons expressing
336 GFP-tagged BoTx compared to the entire population of BoTx-negative dI6 neurons labeled by pTagRFP
337 (Fig. 7C). BoTx-GFP labeled neurons were observed throughout the dorso-ventral range of the dI6
338 population (Fig. 7C, *left and middle*), with a significantly higher proportion observed more ventrally (Fig.
339 7C, middle and *right*). Since dI6 neurons located more ventrally participate in faster swimming
340 movements (Kishore et al., 2020), we expected the impact of synaptic silencing would be more obvious at
341 higher frequencies.

342 Consistent with this idea, in dI6 BoTx-GFP fish we frequently observed synchronous bilateral activity at
343 the beginning of swim episodes when frequency is typically highest (*cf.*, Fig. 1G), which could transition to
344 rhythmic, alternating activity nearer the end of the episode (Fig. 7D). In control larvae, left-right phase
345 values in the first and subsequent swim episodes had peak distributions that rarely deviated from 0.5, as
346 you would expect for perfect alternation during locomotor rhythmogenesis (Fig. 7E, *left*). On the other
347 hand, for BoTx-GFP fish, left-right phase values were more broadly distributed, especially at the
348 beginning of the episode, which was more obvious in the initial swim episode compared to subsequent
349 ones (Fig. 7E, *right*). This is also consistent with differences in peak frequencies observed near the
350 beginning of swim episodes, where they are always higher in the episode immediately following the
351 stimulation (*cf.*, Fig. 1G).

352 The lack of coordinated rhythmogenic output across the body at fast speeds was also apparent when
353 comparing ventral rootlet burst frequencies. In dI6-GFP fish, higher frequency activity overlapping higher
354 frequency activity in controls was observed at the beginning of swim episodes (Fig. 7D, black dots),
355 however this was rarely associated with higher frequency activity in the corresponding cycle on the other

356 side (Fig. 7F). In controls, cyclical frequencies on the left and right side were symmetrical, with most of
357 the datapoints falling along unity (Fig. 7F). Spinal motor neurons exhibit a range of rhythmogenic cellular
358 properties themselves (Menelaou and McLean, 2012), which likely contribute to the higher frequency
359 bursts observed unilaterally. Thus, the disorganized unilateral bursting during bilaterally synchronous
360 output at the onset of swimming in dI6 BoTx-GFP fish is consistent with the selective disruption of
361 rhythmogenesis at fast speeds.

362 Finally, we turned our attention to lower frequency swimming observed nearer the end of swimming,
363 which was less impacted by BoTx expression. For purposes of analysis, we divided the dataset into the
364 initial (Swim 1) and subsequent (Swim 2+) swim episodes, and focused on ventral rootlet burst
365 frequencies below 35 Hz. A comparison of burst frequency and phase revealed no significant differences
366 between dI6 BoTx-GFP and control fish, consistent with a lack of impact on timing and rhythm
367 generation at low frequencies (Fig. 7G-H). However, we did observe an increase in burst duration (Fig.
368 7I), which increased the percentage of the swim cycle occupied by motor output, or duty cycle (Fig. 7J).
369 These effects on were most obvious in the initial swim episode, where duty cycles could reach 90% (Fig.
370 7J). Normally, duty cycles must not exceed 50% of the cycle period to avoid synchronous bilateral
371 contractions during swimming (Grillner, 1974). Thus, at slow speeds the dominant impact of synaptic
372 silencing of dI6 neurons is on motor output, not rhythmogenesis. Collectively, these observations are
373 consistent with the idea that reciprocal inhibition plays a more dominant role in rhythm generation at fast
374 speeds and a more dominant role in pattern formation at slow speeds.

375 **Discussion**

376 Our work was motivated by the opaque origins of spinal rhythmicity at different locomotor speeds and the
377 potential for zebrafish to clarify this fundamental issue. We focused on Chx10-labeled spinal V2a neurons
378 given their conserved role in locomotion in zebrafish and mice (McLean and Dougherty, 2015). In mice,
379 increases in speed involve graded increases in the cyclical frequency of rhythmic activity within limbs and
380 abrupt changes in the coordination between them that define different gaits, like walking, trotting, and
381 bounding (Bellardita and Kiehn, 2015). In larval zebrafish, there are two 'gaits' during forward swimming
382 as defined by limb coordination – slow carangiform mode which involves cyclical abduction/adduction of
383 pectoral fins that alternates across the body and fast anguilliform mode which involves bilateral fin
384 adduction (Thorsen et al., 2004). The transition in fin coordination occurs abruptly between tail beat
385 frequencies of 30-40 Hz in larvae, with graded increases in the cyclical frequency and intensity of body
386 bends leading to increased yaw displacement of the head at faster speeds (Thorsen et al., 2004; McLean et
387 al., 2008).

388 Earlier studies of larval zebrafish found that V2a neurons active at slow speeds are inhibited as V2a
389 neurons active at fast speeds are recruited (McLean et al., 2008). The idea that different gears or modules
390 are responsible for different speeds of locomotion is easier to understand in the context of different gaits.
391 For swimming, faster speeds require not only higher frequency oscillations, but also larger amplitude

body bends that propagate more quickly to generate reactive thrust against the water column for effective propulsion (Grillner, 1974). Among descending V2a neurons, those recruited at faster speeds have longer intersegmental axons (Menelaou et al., 2014) and form stronger connections with other V2a neurons (Menelaou and McLean, 2019). Among bifurcating V2a neurons, intersegmental axon projection distances are more homogeneous, membrane time constants and axon conduction velocities are faster, and connections to motor neurons are stronger and more reliable (Menelaou et al., 2014; Menelaou and McLean, 2019; Menelaou et al., 2022). Thus, as V2a-D neurons with longer axons and V2a-B neurons with stronger premotor connections are engaged at higher frequencies to achieve higher amplitude, faster propagating body bends, V2a neurons whose segmental output is temporally incompatible with fast whole-body coordination are disengaged.

While modular organization makes sense in terms of coordination, the origin of rhythmicity at different speeds was assumed to be the same, whether via cellular properties or synaptic drive or some combination of the two (Marder and Calabrese, 1996; Marder and Bucher, 2001). From our recordings of spinal motor neurons (Menelaou and McLean, 2012; Kishore et al., 2014), we were expecting that cellular properties are more important for rhythmogenesis at slow speeds, while synaptic drive dominates at fast speeds, which could also vary based on V2a type. Our recordings revealed that all V2a neurons demonstrate some form of rhythmicity in response to current steps. The idea that different types of V2a interneurons exhibit different firing properties is not unexpected (Dougherty and Kiehn, 2010; Zhong et al., 2010; Menelaou and McLean, 2019; Song et al., 2020). However, thanks to our ability to link cellular properties to natural recruitment patterns we reveal V2a-Ds alone would qualify as 'pacemakers' (Marder and Calabrese, 1996; Marder and Bucher, 2001), with speed-dependent differences in intrinsic firing mode within V2a-Ds. Specifically, V2a-D neurons recruited at swim frequencies below ~40 Hz during carangiform swimming generate intrinsic bursting at those frequencies, with higher frequency spikes riding atop lower frequency membrane oscillations. Intrinsic oscillations are more sensitive to levels of current injection than spike rates, so increases in tonic excitatory drive would lead to increased burst frequency and thus swim frequency. V2a-D neurons recruited at frequencies above ~40 Hz during anguilliform swimming generate tonic spiking at those frequencies, so increases in tonic excitatory drive would lead to increases in firing frequency and thus swim frequency. In V2a-B neurons, chattering and bursting properties in response to current steps do not reflect their natural firing patterns during swimming, and so we expected they would rely more on pacemaking inputs from V2a-Ds to shape their rhythmicity.

Surprisingly, however, despite clear differences in cellular properties appropriate to generate swimming rhythms, phasic firing in both V2a-Ds and V2a-Bs is best explained by phasic patterns of synaptic excitation and inhibition. Since phasic excitatory input is not tonic and already rhythmic by the time it arrives, this suggests rhythms are generated by more rostral V2a-Ds. Optogenetic stimulation of V2a neurons and spinal lesion studies support a rostral bias in spinal rhythmicity in larval zebrafish (Wiggin et al., 2012; Kimura et al., 2013), consistent with studies of spinal locomotor networks in lampreys and

429 tadpoles, where neurons nearer the hindbrain/spinal cord boundary have a higher capacity for
430 rhythmogenesis (Li et al., 2010; Buchanan, 2018). Our synaptic silencing of dI6 neurons also supports
431 this idea. Previous work using diphtheria toxin to kill dI6 neurons employed an elegant Hox-based
432 strategy to limit expression to the spinal cord (Satou et al., 2020). In contrast to our observations,
433 zebrafish larvae with ablated spinal dI6 neurons can still generate fast swimming. Notwithstanding
434 differences in cellular ablation vs. synaptic silencing approaches and their relative sensitivity to potential
435 compensatory mechanisms (Schnerwitzki et al., 2018; Del Pozo et al., 2020), our strategy also included
436 dI6 neurons that extended into the hindbrain (Fig. 7A, *arrow*). By subtractive reasoning, this argues that
437 reciprocal inhibition nearer the hindbrain/spinal cord is essential for generating high frequency rhythms.

438 Regardless, while all midbody V2a neurons rely on synaptic drive to fire rhythmically at all speeds, the
439 patterns of synaptic excitation and inhibition responsible for rhythmogenesis varies in a cell-type- and
440 speed-dependent manner. Our results combined with prior work allow us to put together a potential
441 model explaining the cellular and synaptic origins of rhythmogenesis at different speeds of swimming. In
442 zebrafish and mice (Hayashi et al., 2018; Menelaou and McLean, 2019), V2a neurons have been
443 categorized into descending (I) and bifurcating (II) subtypes (Fig. 8A, *top*). Our data only strengthen
444 cross-species links by demonstrating that type I and II V2a neurons in larval zebrafish not only differ in
445 axon trajectories, rostro-caudal distribution, size, Chx10-levels, and connectivity, but also in their medio-
446 lateral distribution in the spinal cord (Fig. 1C).

447 Since both V2a subtypes project ipsilaterally, recurrent (or feedback) inhibition must originate from
448 ipsilateral sources, while reciprocal (or feedforward) inhibition originates from commissural sources. In
449 zebrafish, as in mice, there are at least two potential sources of ipsilateral inhibition, V1 neurons
450 (Higashijima et al., 2004) and V2b neurons (Callahan et al., 2019), and two potential sources of
451 commissural inhibition (Satou et al., 2020), dI6 neurons and V0d neurons (Fig. 8A, *bottom*). In our
452 model, we include the two specific types of V2a neurons and single generic sources of recurrent and
453 reciprocal inhibition, each of which has the potential to form connections with the other types (Sengupta
454 and Bagnall, 2023). We do not include conserved sources of commissural excitation here (e.g., V0v and
455 V3 neurons), but these will be important to include in any future models exploring intersegmental
456 coordination and signal amplification (Bohm et al., 2022; Kawano et al., 2022; Wiggin et al., 2022).
457 Notably, the operational definition of reciprocal versus recurrent inhibition would be flipped for
458 commissural excitatory populations, with feedforward inhibition via ipsilateral interneurons and feedback
459 inhibition via commissural interneurons.

460 The simplest scenario is that the wiring diagrams for slow and fast modules are mirror duplications
461 distinguished only by the inclusion of slow or fast motor pools (Fig. 8B). Consistent with this idea, our
462 cell-attached and voltage-clamp data support distinct slow and fast type I V2a-Ds defined by selective
463 within module connectivity. These neurons in turn converge on slow and fast type II V2a-Bs, which relay
464 integrated frequency information to their respective motor pools (Fig. 8C). In the fast module,

465 rhythmogenesis orchestrated by type I V2a neurons relies on reciprocal inhibition. This is consistent with
466 cell-type-specific optical ablation and silencing studies in adult lampreys (Buchanan and McPherson,
467 1995) and embryonic frogs (Moult et al., 2013) that suggest reciprocal inhibition is essential for
468 rhythmogenesis during anguilliform swimming. Rhythmic activity can also be generated in surgically
469 isolated hemi-cords and surgically divided spinal cords of lampreys and frog embryos (Kahn and Roberts,
470 1982; Soffe, 1989; Cangiano and Grillner, 2003, 2005; Li et al., 2010). However, the functional relevance
471 of these rhythms and the impact of lesion-induced plasticity on excitability and connectivity are still
472 debated (Cangiano et al., 2012; Messina et al., 2017; Parker, 2017; Cangiano and Grillner, 2018;
473 McClellan, 2018).

474 In the fast module, recurrent inhibition helps limit motor output via type II V2a-Bs. Type II V2a-Bs have
475 relatively strong connections to motor neurons (Menelaou and McLean, 2019), so limiting their firing
476 would ensure that motor output does not exceed 50% of the duty cycle and risk bilateral co-contraction as
477 the interval between cyclical bursts decreases with increased speed (Grillner, 1974). On the other hand,
478 the cell-type-dependent dominance of reciprocal versus recurrent inhibition is flipped when considering
479 the slow module. Instead, recurrent inhibition is more obvious in type I V2a-D neurons, while type II V2a-
480 B neurons rely exclusively on reciprocal inhibition to pattern their activity (Fig. 8C). Until now recurrent
481 inhibition was linked to limiting motor output (Hultborn et al., 1979), not to rhythmogenesis (see,
482 however, Linden and Berg, 2021).

483 It remains to be seen why reciprocal inhibition would be favored for rhythmogenesis at fast speeds and
484 recurrent inhibition at slow speeds. One possibility is that feedforward inhibition is necessary to properly
485 coordinate bilateral rhythmogenesis among type I V2a-D neurons with longer-range intersegmental
486 connectivity. On the other hand, feedback inhibition among shorter-range type I V2a-D neurons provides
487 an opportunity for local segmental rhythms that rely less on contralateral activity. Since slow type II V2a-
488 B neurons lack feedback inhibition, their recruitment patterns rely exclusively on feedforward inhibition
489 from the opposite side. This means stronger activity on one side should limit output on the other side
490 without impacting timing and vice versa. In support, we recently explored the contribution of spinal V2a
491 neurons to biased swimming during optomotor responses (Jay et al., 2023). We found that type I V2a-D
492 neurons are direction-agnostic, but type II V2a-B neurons are direction-sensitive, with higher recruitment
493 probabilities on the turning side associated with weaker motor output on the opposite side.

494 Interestingly, in contrast to low recruitment probabilities observed for type I V2a-D neurons during
495 swimming evoked by somatosensory stimulation here (<50%; Fig. 5E,F), for swimming during optomotor
496 responses V2a-D neurons are recruited with much higher probabilities (>75%). This is not speed related
497 since swim frequencies during optomotor responses rarely exceeded 35 Hz. Notably, the phase
498 distribution of V2a-D spikes during optomotor responses (Fig. 5H in Jay et al., 2023) better aligns with
499 the phase distribution of EPSCs reported here (Fig. 6C, *bottom*), meaning that type I V2a-Ds fire well in
500 advance of type II V2a-Bs during optomotor responses. Thus, it appears that during somatosensory-

evoked swimming, where intensity and frequency are coupled over a broad range of speeds, type I and type II V2a neurons fire more synchronously than during visually-evoked swimming, where intensity and frequency are uncoupled over a more narrow speed range. While this highlights the modular nature of timing (rhythm) and intensity (pattern) control within the spinal V2a population, future experiments testing this idea will rely on identifying molecular markers that distinguish slow and fast type I and II V2a neurons. Fortunately, recent work has identified promising candidates (Pallucchi et al., 2024).

Another open question is what role differences in cellular properties play during rhythmogenesis. First, our recordings were performed at midbody. It could be that rhythmogenic bursting and spiking properties are a general feature of type I V2a-D neurons, so more rostral neurons have identical cellular properties and rely less on phasic synaptic drive for fast and slow rhythmogenesis. Future recordings from V2a neurons in rostral spinal cord should help resolve this issue, however our dI6 synaptic silencing experiments suggest that reciprocal inhibition will be critical for rostral rhythmogenesis, at least at fast speeds. On the other hand, bursting properties could serve as a source of amplification for synaptic inputs to ensure reliable recruitment of rhythmogenic neurons or provide redundant sources of rhythmogenesis in cases where synaptic drive fails or the spinal cord is damaged. In this sense, cellular properties and synaptic drive would provide synergistic roles amplifying and sharpening rhythmic signals as they propagate segmentally.

In juvenile/adult zebrafish, V2a and motor neurons have been grouped into slow, intermediate, fast and escape modules based on patterns of recruitment and phasic synaptic drive during fictive swimming (El Manira, 2023). In larvae, we also observe recruitment patterns among V2a neurons that would qualify as slow, intermediate, fast and escape based on their criteria (c.f., Fig. 2G). However, we also find that recruitment probability varies based on morphological type, with V2a-D neurons always firing more sparsely than V2a-B neurons, regardless of speed. Thus, low firing probability recorded at slow speeds does not necessarily predict high firing probability at fast speeds. Collectively, these observations suggest that increases in speed in juveniles/adults and larvae are initially accomplished via more reliable V2a neuron recruitment, as also reported in mice (Zhong et al., 2011). This fits studies of motor neurons, where relatively low initial forces rely on recruitment (Enoka and Duchateau, 2017; Jay et al., 2023), while higher forces are achieved by increasing firing rates (Bhatt et al., 2007; Enoka and Duchateau, 2017), in addition to silencing more easily recruited neurons (Smith et al., 1980; Kyriakatos et al., 2011; Menelaou and McLean, 2012).

In sum, our findings suggest that cell-type-specific modes of spinal rhythmogenesis are responsible for different speeds, suggesting a common mechanism of rhythmogenesis is insufficient to explain the full operational range of locomotion. Experiments combining computational modeling with acute segmental perturbations of distinct interneuron types are now needed to explore the functional impact of stratified spinal locomotor circuits with cell-type-specific feedforward and feedback inhibitory motifs.

Materials and methods

537 **Fish husbandry**

538 Tg[Chx10:GFP] fish (ZFIN ID: ZDB-ALT-061204-2) were used to target V2a neurons in the spinal cord
539 (Kimura et al., 2006), and compound Tg[Dmrt3a:Gal4;UAS:pTagRFP] fish (ZFIN IDs: ZDB-FISH-
540 150901-3557; ZDB-TGCONSTRUCT-210826-11) crossed with Tg[UAS:BoTxBLC-GFP] fish (ZFIN ID:
541 ZDB-FISH-160816-31) were used to express botulinum-toxin light chain fused with GFP in commissural
542 inhibitory dI6 interneurons (Satou et al., 2013; Sternberg et al., 2016; Kishore et al., 2020). Fish were
543 maintained at 28.5°C on a 14 hr light/10 hr dark cycle in an aquatics facility staffed by Northwestern
544 University's Center for Comparative Medicine. All experiments were performed at room temperature
545 between 4 and 5 days post fertilization (dpf) when zebrafish larvae are free swimming. Because 4-5 dpf
546 larvae have not yet developed secondary sexual characteristics, their sex cannot be easily determined.
547 Therefore, experiments were performed on larvae of either sex. All experimental protocols conform to
548 National Institutes of Health guidelines on animal experimentation and were approved by the
549 Northwestern University Institutional Animal Care and Use Committee (IS00019359 and IS00019319).

550 **Electrophysiology and analysis**

551 Electrophysiological recordings were acquired using a Multiclamp 700A amplifier (Molecular Devices), a
552 Digidata series 1322A digitizer (Molecular Devices), and pClamp 10 software (Molecular Devices). The
553 intrinsic firing patterns of V2a neurons were assessed by performing 500 ms long current steps at 1-2x
554 rheobase in current-clamp mode. To compare the intrinsic firing properties of V2a neurons to their
555 recruitment profiles during 'fictive' escape swimming, we performed simultaneous whole cell current-
556 clamp recordings of V2a neurons and extracellular recordings of the peripheral ventral rootlet. Synaptic
557 currents during fictive swimming were assessed in dual whole voltage-clamp and extracellular rootlet
558 recordings. Swimming was evoked by applying a mild and brief electrical shock (2-10 V; 0.1-0.4 ms) using
559 a bipolar tungsten electrode placed over the tail fin.

560 For recordings larvae were first paralyzed using alpha-bungarotoxin (1 mg/mL in extracellular solution
561 containing 134 mM NaCl, 2.9 mM KCl, 1.2 mM $MgCl_2$, 10 mM HEPES, 10 mM glucose, and 2.1 mM $CaCl_2$,
562 adjusted to pH 7.8 with NaOH), immersed in extracellular solution containing anesthetic (MS-222), and
563 secured left side up on a Sylgard lined glass bottom dish using custom etched tungsten pins through the
564 notochord. To record the activity of the peripheral ventral rootlets, the skin over the muscle tissue at the
565 midbody was removed using fine forceps. For access to spinal V2a neurons, the muscle tissue over one
566 spinal segment was dissected away using a tool fashioned from sharpened tungsten wire. After the
567 dissection, the preparation was rinsed and immersed in anesthetic-free extracellular solution. For cell-
568 attached and whole cell recordings, standard-wall (1 mm outer diameter) borosilicate capillaries (Sutter
569 Instrument) were pulled to resistances between 5–16 MΩ using a micropipette puller (Flaming/Brown;
570 Sutter Instrument). For peripheral motor nerve recordings, electrodes were made by pulling a patch
571 electrode, breaking the tip, and then heat polishing and bending it using a microforge (MF-830;
572 Narishige) to offset the approach angle for better contact between the electrode and muscle tissue.

573 Peripheral motor nerve recordings were made no more than two segments caudal to the site of cellular
574 recording.

575 For current clamp recordings, patch electrodes were filled with intracellular solution containing (125–130
576 mM K-gluconate, 2–4 mM MgCl2, 0.2–10 mM EGTA, 10 mM HEPES, 4 mM Na2ATP, adjusted to pH 7.3
577 with KOH). For voltage clamp recordings, the intracellular solution consisted of 122 mM $CsMeSO_3$, 0.1–1
578 mM QX314-Cl, 1 mM TEA-Cl, 3 mM $MgCl_2$, 10 mM HEPES, 1 mM EGTA, and 4 mM Na_2-ATP. $CsMeSO_3$
579 and QX-314 Cl were included in the solution to block voltage dependent channels. Alexa Fluor 568
580 hydrazide (50 μmol/l) was also added to the intracellular solution for the post-hoc confirmation of cell
581 identity. Only neurons whose morphologies could be positively identified were included in this study.

582 V2a neurons were targeted on an epifluorescent microscope (Axio Examiner) under a 40×/1.0 NA water-
583 immersion objective (W Plan-Apochromat; Zeiss) using a CCD camera (Rolera-XR; QImaging). The
584 electrode was positioned using a motorized micromanipulator (MP-225; Sutter Instrument or Patchstar,
585 Scientifica), while positive pressure was maintained using a pneumatic transducer (Model DPM-1B; Bio-
586 Tek Instruments) to prevent the tip from clogging as the neuron was approached. The neuron was held at
587 -65 mV during GΩ seal formation. Once the seal was achieved, for voltage-clamp experiments cell
588 attached recordings were performed to obtain the recruitment patterns of V2a neurons during fictive
589 escape swimming before breaking into the neuron to record synaptic currents. A 5 mV hyperpolarizing
590 pulse was then administered at a holding potential of -65 mV, and the steady state current injected during
591 the pulse was used to compute input resistance according to Ohm's law.

592 Excitatory currents were clamped at the reversal potential for inhibition calculated from our solutions,
593 which is -75 mV and inhibitory currents were clamped at the reversal potential for excitation, which is +
594 10 mV. These values were corrected for a calculated junction potential of –11 mV. Thus, neurons were
595 alternately held at the corrected potentials of -64 mV for EPSCs and 21 mV for IPSCs. To monitor series
596 resistance throughout the experiment, recordings were alternately performed without and with 60%
597 series resistance compensation. Standard corrections for bridge balance and electrode capacitance were
598 applied for current clamp recordings. Whole-cell electrical signals were filtered at 10 kHz and digitized at
599 100 kHz at a gain of 10 (feedback resistor, 500 MΩ). Extracellular signals from the peripheral motor
600 nerves were amplified at a gain of 1000 and digitized with low-frequency and high-frequency cutoffs set at
601 300 and 5000 Hz, respectively.

602 Whole cell and extracellular recordings were annotated in Dataview to label individual spikes, ventral
603 rootlet bursts and swimming episodes. The onset and duration of spikes, ventral root bursts and
604 swimming episodes were then batch exported into text files, which were then read into MATLAB
605 (Mathworks) for further analysis. Instantaneous spike frequencies are the inverse of the period between
606 two successive action potentials. The recruitment patterns of V2a neurons were quantified by computing
607 the probability of observing spikes for all cycles present within each 5 Hz ventral root burst frequency bin
608 from 10 Hz to 65 Hz. The recruitment probability was then plotted as a function of ventral root burst

609 frequency. The V2a neurons with an upward sloping recruitment reliability plot were classified as fast and
610 those with a downward sloping plot were categorized as slow (cf. trendlines in Fig. 4E)

611 Maximum excitatory and inhibitory currents reflect the maximum current received at any ventral root
612 burst frequency. To compare frequency dependent changes in synaptic currents across neuron types, they
613 were normalized against the maximum synaptic current the neuron received. Normalized currents were
614 then averaged in four discrete frequency bins spanning carangiform and anguilliform swimming modes
615 (15-25, 25-35, 35-45, 45+ Hz). To analyze the phasic timing of spiking and synaptic currents, they were
616 normalized to the period of the corresponding cycle, such that the centers of successive motor bursts
617 marked phase 0 and phase 1. Synaptic currents arriving between 0.75 to 0.25 , were considered in-phase
618 and those between 0.25 and 0.75 considered anti-phase. To analyze the relative timing of excitation and
619 inhibition, we normalized amplitudes to the maximum current received in each cycle, such that the final
620 values of normalized current ranged between 0 and 1. Currents were then averaged for all cycles present
621 within the four frequency bins

622 To quantify peaks in synaptic currents corresponding to the phasic inputs received during a swim cycle,
623 current traces were low pass filtered at the cutoff frequency of 1000 Hz using the butterworth (second
624 order) and zero phase digital filters in MATLAB. The latter was used to prevent the raw current values
625 from undergoing a phase shift. Peaks were detected using the findpeaks() function in MATLAB. Counts of
626 V2a spikes, EPSC's and IPSC's were plotted on a circular axis from phase 0 to 1. Data visualization and
627 statistical analysis were performed in R.

628 To quantify left-right alternation in control and botulinum-toxin expressing dI6 neurons, dual ventral
629 rootlet recordings were rectified and annotated in DataView. Owing to the highly irregular nature of the
630 ventral rootlet activity in the dI6-silenced fish, automatic event detection parameters used to distinguish
631 motor bursts in control conditions were unable to accurately demarcate the boundaries of motor bursts in
632 BoTx-GFP fish. Therefore, all annotations for controls and BoTx-GFP were performed manually. Ventral
633 root bursts at frequencies above a 100 Hz were excluded from analysis since this is the upper bound of
634 their natural swimming range (Muller and van Leeuwen, 2004). Stimulus, burst and bout onset and offset
635 times for all recordings were batch exported into text files. Custom written MATLAB code was then used
636 to classify Swim 1 and Swim 2+ episodes and identify corresponding bursts in the dual ventral rootlet
637 recordings to compute phase values. Phase values were calculated from the center of the ventral rootlet
638 motor burst.

639 **Imaging and analysis**

640 After each electrophysiological recording, a series of epifluorescent and differential interference contrast
641 images were captured using a CCD camera (Rolera-XR) and QCapture Suite imaging software (QImaging)
642 to track the axonal trajectories of V2a neurons and confirm their morphology. Images were later analyzed
643 in ImageJ. Confocal z-stacks of Tg[Chx10:GFP] and Tg[Dmrt3a:GFP] fish were captured on using a Zeiss
644 LSM710 microscope using established protocols (Menelaou et al., 2014).

645 Soma size and dorsoventral locations of individually labeled V2a neurons were measured in ImageJ.
646 Dorsoventral (DV) and mediolateral (ML) positions of V2a neurons in Tg[Chx10:GFP] were computed by
647 obtaining the relevant positional coordinates from confocal images in Imaris (Oxford Instruments).
648 Briefly, the spot detection tool was used to obtain the coordinates of the centers of all somata and
649 orthogonal slicers were used in conjunction with measurement points to extract the coordinates of the
650 dorsoventral and lateral boundaries of the spinal cord as well as the central canal. The positions of the
651 somata were then respectively normalized against the positions of the dorsoventral and mediolateral
652 boundaries to get the final DV and ML positions. V2a somata were classified into two groups based on the
653 intensity of GFP expression. The GFP fluorescence intensity of V2a somata was exported from Imaris, and
654 its density distribution was plotted in R. Because the density distribution of GFP fluorescence intensity
655 was bimodal, the minimum between the two modes of the distribution was used as a cut off to split V2a
656 neurons into classes of low and high GFP expression. Dorsoventral positions of dI6 neurons in compound
657 Tg[Dmrt3a:Gal4;UAS:pTagRFP] x Tg[UAS:BoTxBLC-GFP] larvae were calculated using the relevant
658 positional coordinates from confocal images in Imaris and normalizing them to the dorsal and ventral
659 boundaries of spinal cord determined using differential contrast images.

660 **High speed filming**

661 To illustrate the differences in body shape and frequency with time, we include a video of a freely
662 swimming 5 day old larva captured at 2000 frames/sec using a FASTCAM Mini AX50 (Photron), evoked
663 using a sharpened tungsten pin to stimulate somatosensory afferents (Video 1).

664 **Statistics**

665 All data were first tested for normality to select the appropriate statistical test. None of the data were
666 normally distributed, so nonparametric tests were used to assess statistical significance. The difference
667 between the density distributions of mediolateral and dorsoventral somatic positions was tested using the
668 Two-sample Kolmogorov-Smirnov test. Correlations were measured using Spearman's rank correlation
669 test. Comparisons between two groups of paired or unpaired data were performed using the Wilcoxon
670 signed-rank test and the Wilcoxon rank sum test, respectively. For data comprised of more than two
671 groups, differences were assessed using the Kruskal-Wallis test, followed by pairwise comparisons using
672 Dunn's test with a post-hoc Benjamini-Hochberg false-discovery rate (FDR) correction for multiple
673 comparisons. For circular plots, Watson's two-sample test of homogeneity was used to determine whether
674 the spike and post synaptic current distributions in two conditions were significantly different from each
675 other. Statistically significant differences are denoted as follows: $*p < 0.05$; $**p < 0.01$; $***p < 0.001$. Note
676 that it was not always possible to collect cell-attached data and voltage-clamp recordings of excitation and
677 inhibition in the same cells, so n numbers reported in the text can vary between conditions. The same
678 holds true for measured parameters in current-clamp recordings, where soma size, dorso-ventral position,
679 input resistance, rheobase, spike rates, and recruitment order in the same neurons were not always
680 possible.

681 **References**

682 Ausborn J, Shevtsova NA, Caggiano V, Danner SM, Rybak IA (2019) Computational modeling of
683 brainstem circuits controlling locomotor frequency and gait. Elife 8:e43587.
684 Bellardita C, Kiehn O (2015) Phenotypic characterization of speed-associated gait changes in mice reveals
685 modular organization of locomotor networks. Curr Biol 25:1426-1436.
686 Bello-Rojas S, Istrate AE, Kishore S, McLean DL (2019) Central and peripheral innervation patterns of
687 defined axial motor units in larval zebrafish. J Comp Neurol 527:2557-2572.
688 Bhatt DH, McLean DL, Hale ME, Fetcho JR (2007) Grading movement strength by changes in firing
689 intensity versus recruitment of spinal interneurons. Neuron 53:91-102.
690 Bhattacharyya K, McLean DL, MacIver MA (2021) Intersection of motor volumes predicts the outcome of
691 ambush predation of larval zebrafish. J Exp Biol 224:jeb235481.
692 Bohm UL, Kimura Y, Kawashima T, Ahrens MB, Higashijima SI, Engert F, Cohen AE (2022) Voltage
693 imaging identifies spinal circuits that modulate locomotor adaptation in zebrafish. Neuron
694 110:1211-1222 e1214.
695 Brocard F, Tazerart S, Vinay L (2010) Do pacemakers drive the central pattern generator for locomotion
696 in mammals? Neuroscientist 16:139-155.
697 Brown TG (1911) The intrinsic factors in the act of progression in the mammal. Proc R Soc B – Biol Sci
698 84:308-319.
699 Buchanan JT (2018) Swimming rhythm generation in the caudal hindbrain of the lamprey. J
700 Neurophysiol 119:1681-1692.
701 Buchanan JT, McPherson DR (1995) The neuronal network for locomotion in the lamprey spinal cord:
702 evidence for the involvement of commissural interneurons. J Physiol Paris 89:221-233.
703 Budick SA, O'Malley DM (2000) Locomotor repertoire of the larval zebrafish: swimming, turning and
704 prey capture. J Exp Biol 203:2565-2579.
705 Burke RE, Degtyarenko AM, Simon ES (2001) Patterns of locomotor drive to motoneurons and last-order
706 interneurons: clues to the structure of the CPG. J Neurophysiol 86:447-462.
707 Callahan RA, Roberts R, Sengupta M, Kimura Y, Higashijima SI, Bagnall MW (2019) Spinal V2b neurons
708 reveal a role for ipsilateral inhibition in speed control. Elife 8.
709 Cangiano L, Grillner S (2003) Fast and slow locomotor burst generation in the hemispinal cord of the
710 lamprey. J Neurophysiol 89:2931-2942.
711 Cangiano L, Grillner S (2005) Mechanisms of rhythm generation in a spinal locomotor network deprived
712 of crossed connections: the lamprey hemicord. J Neurosci 25:923-935.
713 Cangiano L, Grillner S (2018) Commentary: elimination of left-right reciprocal coupling in the adult
714 lamprey spinal cord abolishes the generation of locomotor activity. Front Neural Circuits 12:34.
715 Cangiano L, Hill RH, Grillner S (2012) The hemisegmental locomotor network revisited. Neuroscience
716 210:33-37.

717 D'Elia KP, Hameedy H, Goldblatt D, Frazel P, Kriese M, Zhu Y, Hamling KR, Kawakami K, Liddelow SA,
718 Schoppik D, Dasen JS (2023) Determinants of motor neuron functional subtypes important for
719 locomotor speed. Cell Rep 42:113049.
720 Del Pozo A, Manuel R, Iglesias Gonzalez AB, Koning HK, Habicher J, Zhang H, Allalou A, Kullander K,
721 Boije H (2020) Behavioral characterization of dmrt3a mutant zebrafish reveals crucial aspects of
722 vertebrate locomotion through phenotypes related to acceleration. eNeuro 7.
723 Di Santo V, Goerig E, Wainwright DK, Akanyeti O, Liao JC, Castro-Santos T, Lauder GV (2021)
724 Convergence of undulatory swimming kinematics across a diversity of fishes. Proc Natl Acad Sci
725 U S A 118:e2113206118.
726 Dougherty KJ, Kiehn O (2010) Firing and cellular properties of V2a interneurons in the rodent spinal
727 cord. J Neurosci 30:24-37.
728 El Manira A (2023) Modular circuit organization for speed control of locomotor movements. Curr Opin
729 Neurobiol 82:102760.
730 Enoka RM, Duchateau J (2017) Rate coding and the control of muscle force. Cold Spring Harb Perspect
731 Med 7.
732 Grillner S (1974) On the generation of locomotion in the spinal dogfish. Exp Brain Res 20:459-470.
733 Grillner S (1981) Control of locomotion in bipeds, tetrapods, and fish. In: Handbook of Physiology, The
734 Nervous System, Motor Control (Terjung R, ed).
735 Grillner S (1985) Neurobiological bases of rhythmic motor acts in vertebrates. Science 228:143-149.
736 Grillner S, Kozlov A (2021) The CPGs for limbed locomotion-facts and fiction. Int J Mol Sci 22:5882.
737 Guertin PA (2009) The mammalian central pattern generator for locomotion. Brain Res Rev 62:45-56.
738 Hayashi M, Hinckley CA, Driscoll SP, Moore NJ, Levine AJ, Hilde KL, Sharma K, Pfaff SL (2018) Graded
739 arrays of spinal and supraspinal V2a interneuron subtypes underlie forelimb and hindlimb motor
740 control. Neuron 97:869-884 e865.
741 Higashijima S, Masino MA, Mandel G, Fetcho JR (2004) Engrailed-1 expression marks a primitive class
742 of inhibitory spinal interneuron. J Neurosci 24:5827-5839.
743 Hultborn H, Lindstrom S, Wigstrom H (1979) On the function of recurrent inhibition in the spinal cord.
744 Exp Brain Res 37:399-403.
745 Jay M, MacIver MA, McLean DL (2023) Spinal basis of direction control during locomotion in larval
746 zebrafish. J Neurosci 43:4062-4074.
747 Kahn JA, Roberts A (1982) Experiments on the central pattern generator for swimming in amphibian
748 embryos. Philos Trans R Soc Lond B Biol Sci 296:229-243.
749 Kawano K, Kato K, Sugioka T, Kimura Y, Tanimoto M, Higashijima SI (2022) Long descending
750 commissural Vov neurons ensure coordinated swimming movements along the body axis in larval
751 zebrafish. Sci Rep 12:4348.
752 Kimura Y, Okamura Y, Higashijima S (2006) alx, a zebrafish homolog of Chx10, marks ipsilateral
753 descending excitatory interneurons that participate in the regulation of spinal locomotor circuits.
754 J Neurosci 26:5684-5697.

755 Kimura Y, Satou C, Fujioka S, Shoji W, Umeda K, Ishizuka T, Yawo H, Higashijima S (2013) Hindbrain
756 V2a neurons in the excitation of spinal locomotor circuits during zebrafish swimming. Curr Biol
757 23:843-849.
758 Kishore S, Bagnall MW, McLean DL (2014) Systematic shifts in the balance of excitation and inhibition
759 coordinate the activity of axial motor pools at different speeds of locomotion. J Neurosci
760 34:14046-14054.
761 Kishore S, Cadoff EB, Agha MA, McLean DL (2020) Orderly compartmental mapping of premotor
762 inhibition in the developing zebrafish spinal cord. Science 370:431-436.
763 Koshland GF, Smith JL (1989) Mutable and immutable features of paw-shake responses after hindlimb
764 deafferentation in the cat. J Neurophysiol 62:162-173.
765 Kozlov A, Huss M, Lansner A, Kotaleski JH, Grillner S (2009) Simple cellular and network control
766 principles govern complex patterns of motor behavior. Proc Natl Acad Sci U S A 106:20027-
767 20032.
768 Kriellaars DJ, Brownstone RM, Noga BR, Jordan LM (1994) Mechanical entrainment of fictive
769 locomotion in the decerebrate cat. J Neurophysiol 71:2074-2086.
770 Kyriakatos A, Mahmood R, Ausborn J, Porres CP, Buschges A, El Manira A (2011) Initiation of locomotion
771 in adult zebrafish. J Neurosci 31:8422-8431.
772 Lafreniere-Roula M, McCrea DA (2005) Deletions of rhythmic motoneuron activity during fictive
773 locomotion and scratch provide clues to the organization of the mammalian central pattern
774 generator. J Neurophysiol 94:1120-1132.
775 Li WC, Roberts A, Soffe SR (2010) Specific brainstem neurons switch each other into pacemaker mode to
776 drive movement by activating NMDA receptors. J Neurosci 30:16609-16620.
777 Linden H, Berg RW (2021) Why firing rate distributions are important for understanding spinal central
778 pattern generators. Front Hum Neurosci 15:719388.
779 Marder E, Calabrese RL (1996) Principles of rhythmic motor pattern generation. Physiol Rev 76:687-717.
780 Marder E, Bucher D (2001) Central pattern generators and the control of rhythmic movements. Curr Biol
781 11:R986-996.
782 McClellan AD (2018) Response: commentary: elimination of left-right reciprocal coupling in the adult
783 lamprey spinal cord abolishes the generation of locomotor activity. Front Neural Circuits 12:62.
784 McCrea DA, Rybak IA (2008) Organization of mammalian locomotor rhythm and pattern generation.
785 Brain Res Rev 57:134-146.
786 McHenry MJ, Lauder GV (2006) Ontogeny of form and function: locomotor morphology and drag in
787 zebrafish (Danio rerio). J Morphol 267:1099-1109.
788 McLean DL, Fetcho JR (2009) Spinal interneurons differentiate sequentially from those driving the
789 fastest swimming movements in larval zebrafish to those driving the slowest ones. J Neurosci
790 29:13566-13577.
791 McLean DL, Dougherty KJ (2015) Peeling back the layers of locomotor control in the spinal cord. Curr
792 Opin Neurobiol 33:63-70.

793 McLean DL, Fan J, Higashijima S, Hale ME, Fetcho JR (2007) A topographic map of recruitment in
794 spinal cord. Nature 446:71-75.
795 McLean DL, Masino MA, Koh IY, Lindquist WB, Fetcho JR (2008) Continuous shifts in the active set of
796 spinal interneurons during changes in locomotor speed. Nat Neurosci 11:1419-1429.
797 Menelaou E, McLean DL (2012) A gradient in endogenous rhythmicity and oscillatory drive matches
798 recruitment order in an axial motor pool. J Neurosci 32:10925-10939.
799 Menelaou E, McLean DL (2019) Hierarchical control of locomotion by distinct types of spinal V2a
800 interneurons in zebrafish. Nat Commun 10:4197.
801 Menelaou E, VanDunk C, McLean DL (2014) Differences in the morphology of spinal V2a neurons reflect
802 their recruitment order during swimming in larval zebrafish. J Comp Neurol 522:1232-1248.
803 Menelaou E, Kishore S, McLean DL (2022) Mixed synapses reconcile violations of the size principle in
804 zebrafish spinal cord. Elife 11.
805 Messina JA, St Paul A, Hargis S, Thompson WE, McClellan AD (2017) Elimination of left-right reciprocal
806 coupling in the adult lamprey spinal cord abolishes the generation of locomotor activity. Front
807 Neural Circuits 11:89.
808 Moult PR, Cottrell GA, Li WC (2013) Fast silencing reveals a lost role for reciprocal inhibition in
809 locomotion. Neuron 77:129-140.
810 Muller UK, van Leeuwen JL (2004) Swimming of larval zebrafish: ontogeny of body waves and
811 implications for locomotory development. J Exp Biol 207:853-868.
812 Myers P, Eisen J, Westerfield M (1986) Development and axonal outgrowth of identified motorneurons in
813 the zebrafish. J Neurosci 6:2278-2289.
814 Pallucchi I, Bertuzzi M, Madrid D, Fontanel P, Higashijima SI, El Manira A (2024) Molecular blueprints
815 for spinal circuit modules controlling locomotor speed in zebrafish. Nat Neurosci 27:78-89.
816 Parker D (2017) The lesioned spinal cord is a “new" spinal cord: evidence from functional changes after
817 spinal injury in lamprey. Front Neural Circuits 11:84.
818 Patterson BW, Abraham AO, MacIver MA, McLean DL (2013) Visually guided gradation of prey capture
819 movements in larval zebrafish. J Exp Biol 216:3071-3083.
820 Perret C, Cabelguen JM (1980) Main characteristics of the hindlimb locomotor cycle in the decorticate cat
821 with special reference to bifunctional muscles. Brain Res 187:333-352.
822 Picton LD, Bjornfors ER, Fontanel P, Pallucchi I, Bertuzzi M, El Manira A (2022) Developmental switch
823 in the function of inhibitory commissural V0d interneurons in zebrafish. Curr Biol 32:3515-3528.
824 Russell DF, Wallen P (1983) On the control of myotomal motoneurones during "fictive swimming" in the
825 lamprey spinal cord in vitro. Acta Physiol Scand 117:161-170.
826 Ryczko D, Dubuc R, Cabelguen JM (2010) Rhythmogenesis in axial locomotor networks: an interspecies
827 comparison. Prog Brain Res 187:189-211.
828 Satou C, Kimura Y, Hirata H, Suster ML, Kawakami K, Higashijima S (2013) Transgenic tools to
829 characterize neuronal properties of discrete populations of zebrafish neurons. Development
830 140:3927-3931.

831 Satou C, Sugioka T, Uemura Y, Shimazaki T, Zmarz P, Kimura Y, Higashijima SI (2020) Functional
832 diversity of glycinergic commissural inhibitory neurons in larval zebrafish. Cell Rep 30:3036-
833 3050.
834 Schnerwitzki D, Perry S, Ivanova A, Caixeta FV, Cramer P, Gunther S, Weber K, Tafreshiha A, Becker L,
835 Vargas Panesso IL, Klopstock T, Hrabe de Angelis M, Schmidt M, Kullander K, Englert C (2018)
836 Neuron-specific inactivation of Wt1 alters locomotion in mice and changes interneuron
837 composition in the spinal cord. Life Sci Alliance 1:e201800106.
838 Sengupta M, Bagnall MW (2023) Spinal interneurons: diversity and connectivity in motor control. Annu
839 Rev Neurosci 46:79-99.
840 Smith JL, Betts B, Edgerton VR, Zernicke RF (1980) Rapid ankle extension during paw shakes: selective
841 recruitment of fast ankle extensors. J Neurophysiol 43:612-620.
842 Soffe SR (1989) Roles of glycinergic Inhibition and N-methyl-D-aspartate receptor mediated excitation in
843 the locomotor rhythmicity of one half of the Xenopus embryo central nervous system. Eur J
844 Neurosci 1:561-571.
845 Soffe SR, Roberts A (1982) Tonic and phasic synaptic input to spinal cord motoneurons during fictive
846 locomotion in frog embryos. J Neurophysiol 48:1279-1288.
847 Song J, Pallucchi I, Ausborn J, Ampatzis K, Bertuzzi M, Fontanel P, Picton LD, El Manira A (2020)
848 Multiple rhythm-generating circuits act in tandem with pacemaker properties to control the start
849 and speed of locomotion. Neuron 105:1048-1061.
850 Soto AP, McHenry MJ (2020) Pursuit predation with intermittent locomotion in zebrafish. J Exp Biol
851 223:jeb230623.
852 Sternberg JR, Severi KE, Fidelin K, Gomez J, Ihara H, Alcheikh Y, Hubbard JM, Kawakami K, Suster M,
853 Wyart C (2016) Optimization of a neurotoxin to investigate the contribution of excitatory
854 interneurons to speed modulation in vivo. Curr Biol 26:2319-2328.
855 Talpalar AE, Bouvier J, Borgius L, Fortin G, Pierani A, Kiehn O (2013) Dual-mode operation of neuronal
856 networks involved in left-right alternation. Nature 500:85-88.
857 Thorsen DH, Cassidy JJ, Hale ME (2004) Swimming of larval zebrafish: fin-axis coordination and
858 implications for function and neural control. J Exp Biol 207:4175-4183.
859 Wiggin TD, Anderson TM, Eian J, Peck JH, Masino MA (2012) Episodic swimming in the larval zebrafish
860 is generated by a spatially distributed spinal network with modular functional organization. J
861 Neurophysiol 108:925-934.
862 Wiggin TD, Montgomery JE, Brunick AJ, Peck JH, Masino MA (2022) V3 Interneurons Are Active and
863 Recruit Spinal Motor Neurons during In Vivo Fictive Swimming in Larval Zebrafish. eNeuro 9.
864 Zhong G, Sharma K, Harris-Warrick RM (2011) Frequency-dependent recruitment of V2a interneurons
865 during fictive locomotion in the mouse spinal cord. Nat Commun 2:274.
866 Zhong G, Droho S, Crone SA, Dietz S, Kwan AC, Webb WW, Sharma K, Harris-Warrick RM (2010)
867 Electrophysiological characterization of V2a interneurons and their locomotor-related activity in
868 the neonatal mouse spinal cord. J Neurosci 30:170-182.

869 Ziskind-Conhaim L, Hochman S (2017) Diversity of molecularly defined spinal interneurons engaged in
870 mammalian locomotor pattern generation. J Neurophysiol 118:2956-2974.

871

872

873 **Figure legends**

874

875 **Figure 1: Identification of V2a neurons for recordings during 'fictive' swimming**

876 **A)** Composite DIC/epifluorescence image of Tg[Chx10:GFP] larval zebrafish at 5 days post fertilization
877 (5d). Dorsal is up and rostral is left. Scale bar, 0.5 mm.

878 **B)** Confocal image of the Tg[Chx10:GFP] spinal cord from segments 10-15 at midbody (purple box in *A*).
879 Scale bar, 30 µm.

880 **C)** Pseudo-colored images of V2a somata based on high (H, white) and low (L, purple) GFP intensity. Left
881 panel: sagittal section, right panel: coronal section. Dashed lines indicate boundaries of spinal cord,
882 which are normalized to 0-1 in the dorso-ventral (DV) and medio-lateral (ML) axes. White arrowheads
883 indicate large, lateral V2a somata with low levels of GFP expression. Scale bar, 20 µm.

884 **D)** Plots of numbers of low and high intensity V2a neurons per midbody segment (n = 5-6 segments from
885 3 fish). Left panel: Bar plot of average number (+/- SEM) of low and high GFP V2a neurons along the
886 dorsoventral (DV) axis. There is no significant difference in the medians of the dorso-ventral
887 distributions of high and low GFP expressing V2a neurons (Wilcoxon rank-sum rest; W = 684, p =
888 0.698, n = 347 high and 401 low GFP neurons from 3 fish). Right panel: Box and whisker plot showing
889 average number of high and low GFP neurons per segment (Wilcoxon rank-sum test; W = 88, p =
890 0.053, n = 17 segments in 3 fish).

891 **E)** Two-dimensional contour density plots showing the mediolateral (ML) and dorsoventral (DV)
892 distributions of V2a neurons expressing low or high levels of GFP. Density distributions of ML
893 positions of V2a neurons are shown at the bottom of the contour plots, which are significantly different
894 (***, Two-sample Kolmogorov-Smirnov test; D = 0.164 p <0.001, n = 347 high and 401 low GFP
895 neurons from 3 fish).

896 **F)** Top panel: an example of an extracellular ventral rootlet recording of three consecutive swim episodes
897 evoked by a mild electrical stimulus (s) to the tail fin (at arrowhead, artifact blanked). Scale bar, 500
898 ms. Bottom left panel: a cartoon of the locations of the stimulus and the recording electrodes. Bottom
899 right panel: individual ventral rootlet bursts (vrb) on an expanded timescale. Black dots mark the
900 center of each vrb used to calculate swim frequency in Hz (1/s), which is indicative of swimming speed.
901 Scale bar, 20 ms.

902 **G)** Scatter plot of vrb frequency (Hz) versus the time in swim episode (ms). The swimming episode
903 immediately following the stimulus is called Swim 1 (left), and any subsequent swimming episodes are
904 called Swim 2+ (right).

905

906 **Figure 2: Cell-type-specific electrophysiological properties linked to recruitment order**

907 **A)** Composite DIC/epifluorescent images of post-hoc fills of V2a-Descending (V2a-D, top) and V2a-
908 Bifurcating (V2a-B, bottom) neurons. Arrows indicate continuation of axons outside the field of view.
909 Scale bar, 10 µm.

B) Left panel: scatter plot of soma diameter of V2a-D and V2a-B neurons normalized to dorsoventral (DV) soma position, with 1 demarcating the dorsal and 0 the ventral boundaries of the spinal cord. The soma diameters of V2a-Ds (n = 22) and V2a-Bs (n = 25) are significantly different according to the Wilcoxon rank-sum test (W = 401, $p < 0.001$). Right panel: boxplots of DV soma positions of V2a-D and V2a-B neurons classified as tonic, bursting, or chattering based on their step-firing responses in panels *E* and *F*. TD=tonic V2a-D (n = 14), CB=chattering V2a-B (n = 12), BB=bursting V2a-B (n = 13), BD=bursting V2a-D (n = 8). The differences in the DV soma positions of TD and CB (z = -3.202, $p < 0.01$), TD and BB (z = -4.714, $p < 0.001$), and TD and BD (z = -4.892, $p < 0.001$) are significantly different according to Dunn's test following post-hoc Benjamini-Hochberg correction.

C) Left panel: scatter plot of input resistance (GΩ) versus the rheobase (pA) of V2a-B (black) and V2a-D (blue) neurons. The input resistance (W = 30, $p < 0.001$) and rheobase (W = 361.5, $p < 0.001$) of V2a-Bs (n = 18) and V2a-Ds (n = 21) are significantly different according to the Wilcoxon rank-sum test. Right panel: Box plots of input resistance (GΩ) of BD (n = 7), TD (n =14), BB (n = 11), and CB (n = 7) V2a neurons. The differences in the input resistance of BD and BB (z = -3.531, $p < 0.001$), BD and CB (z = 4.734, $p < 0.001$), CB and TD neurons (z = -3.559, $p < 0.01$) are significantly different according to Dunn's test following post-hoc Benjamini-Hochberg correction.

D) Mean (+/– SD) instantaneous spike rates (Hz) between 1-2x rheobase for TD, CB, BD and BB neurons.

E) Top panel: step-firing responses of V2a-D neurons defined as tonic (TD). Bottom panel: step-firing responses of V2a-D neurons defined as bursting (BD). Grey dots depict the midpoint of slower membrane oscillations driving the bursting spiking behavior. Same scale as panel *F*.

F) Top panel: step-firing responses of V2a-B neurons defined as chattering (CB). Bottom panel: V2a-B neurons defined as bursting (BB). Grey dots depict the midpoint of slower membrane oscillations driving the bursting spiking behavior. Scale bars, 20 mV, 200 pA, 200 ms.

G) Top panels: Step-firing responses close to rheobase of TD, BD, CB, and BB neurons. Bottom panels: Swim firing responses evoked by a mild electrical shock shown on the same time scales. Black dots on ventral root bursts (grey) indicate swim frequency. Black arrows mark the stimulation artifact. Scale bars, 10 mV, 50 ms.

H) Scatter plot of median swim firing frequency (Hz) versus the input resistance (GΩ) of CB, TD, BB, and BD on logarithmic x- and y-scales. Shaded grey box indicates 30-40 Hz range reflecting transition between anguilliform and carangiform swim modes. There is a significant negative correlation between the median swim firing frequency and input resistance of TD and BD V2a neurons (Spearman's rank correlation test, r_s = -0.723, $p < 0.001$, n = 21) as well as CB and BB V2a neurons (r_s = -0.624, $p < 0.01$, n = 18).

I) A comparison of median swim-firing and median step-firing frequencies between 1-2x rheobase (+/– SD) for TD, BD, and BB neurons. For TD neurons, step frequencies represent spike rates, while for BD and BB neurons they represent burst rates. CB neurons were too variable in step firing frequency to obtain reliable median values. Shaded grey box indicates 30-40 Hz range reflecting transition between anguilliform and carangiform swim modes. There is a significant positive correlation between the

948 median swim-firing and median step-firing frequencies of TD and BD neurons (Spearman's rank
949 correlation test; r_s = 0.768, p <0.001, n = 21), but not BB neurons (Spearman's rank correlation test;
950 r_s = 0.318, p = 0.289, n = 13).
951
952 **Figure 3: Differences in recruitment patterns among the distinct V2a types**
953 **A)** Left panel: Cell-attached (ca) recordings of descending V2a (V2a-D) neurons during fictive swimming
954 evoked by a brief stimulus (at black arrowhead). Black dots on ventral root (vr) bursts (grey) indicate
955 swim frequency. The top neuron fires immediately after the stimulus during high frequency
956 swimming, while the bottom neuron fires near the end of the episode at lower frequencies. Right
957 panel: As shown to the left, but for bifurcating V2a (V2a-B) neurons. Scale bar, 100 ms.
958 **B)** Top panel: spike timing of V2a-D (left) and V2a-B (right) neurons relative to the start of swimming
959 ordered by the median of the distribution. Bottom panel: A scatterplot of vrb frequency (Hz) as a
960 function of time for all episodes (Swim 1 and 2+) during which the V2a-D (left) or V2a-B (right)
961 neurons were recruited.
962 **C)** Raster plots of ventral root burst frequencies (Hz) over which V2a-Ds were recruited ordered by the
963 median vrb recruitment frequency (Hz). Shaded box indicates 30-40 Hz range reflecting transition
964 between anguilliform and carangiform swim modes.
965 **D)** Raster plots of ventral root burst frequencies (Hz) over which V2a-Bs were recruited ordered by the
966 median vrb recruitment frequency (Hz). Shaded box indicates 30-40 Hz range reflecting transition
967 between anguilliform and carangiform swim modes.
968
969 **Figure 4: Distinct types of slow and fast V2a neurons distinguished based on recruitment**
970 **A)** Top panel: Cell-attached (ca) and ventral rootlet (vr) recordings during slow (<35 Hz) and fast (>35
971 Hz) swimming illustrate V2a-D neurons (blue) that fire exclusively at slow and fast speeds. Bottom
972 panel: V2a-B neurons (black) fire more reliably at both slow and fast speeds. Scale bar, 25 ms.
973 **B)** Plots of the mean (+/– SD) dorsoventral (DV) positions of fast (FD) and slow (SD) V2a-Ds, and fast
974 (FB) and slow (SB) V2a-Bs versus their mean (+/– SD) input resistance (Rin).
975 **C)** Spike timing of slow (S) and fast (F) V2a-D and V2a-B neurons relative to the center of the ventral root
976 burst (vrb) depicted by the dashed vertical line. Tick marks represent individual spikes from multiple
977 cycles and circles represent median spike timing.
978 **D)** Density plots of spike timing relative to the center burst for slow and fast V2a-B and V2a-D neurons
979 illustrated in panel *C*.
980 **E)** Top panel: Box plots of the percentage of ventral root bursts with spikes (vrb spikes %) as a function of
981 vrb frequency (Hz) for fast (FD, n = 9) and slow (SD, n = 8) V2a-D neurons. For box plots, the ventral
982 root burst frequency was binned at 15 Hz intervals starting at 15 Hz, and the final interval of 45+Hz
983 consisted of a 20 Hz range spanning from 45-65 Hz. Box plots are superimposed on trendlines from
984 individual neurons fit to data binned at 5 Hz intervals, whose slopes define whether they are fast

(positive) or slow (negative). Dashed line indicates transition between slow carangiform and fast anguilliform modes. Bottom panel: As above but for fast (FB, n = 16) and slow (SB, n = 6) V2a-B neurons.

F) Top panel: Box plots of vrb spikes % for slow and fast V2a-D neurons from panel E collapsed into single slow (<35 Hz) and (>35 Hz) bins for purposes of statistical analysis (Wilcoxon signed-rank test; FD, V = 1, p <0.01, n = 9; SD, V = 36, p = < 0.01, n = 8). Bottom panel: As above but for V2a-B neurons (Wilcoxon signed-rank test; FB, V = 0, p <0.001, n = 16; SB, V = 20, p = 0.063, n = 6).

G) Top panel: Scatter plots of instantaneous spike rates versus vrb frequency (Hz) for V2a-D (left) and V2a-B (right) neurons color coded as fast (dark) and slow (light). FD, n = 9; SD, n = 8; FB, n = 16; SB; n = 6, Bottom panel: Scatter plots of the number of spikes per ventral root burst (#) as a function of vrb frequency (Hz), organized and color coded as above.

H) Top panel: Box plots of maximum instantaneous spike rates for fast (n = 5) and slow (n = 7) V2a-D and fast (n = 16) and slow (n = 5) V2a-B neurons. Note, only a subset of V2a neurons that fired two or more spikes per cycle were included in this analysis (Wilcoxon rank-sum test; FB-FD, W = 73, p <0.01; FB-SD, W = 90, p < 0.05). Bottom panel: Box plots of the maximum number of spikes/vrb (Wilcoxon rank-sum test; FB-FD, W = 133, p <0.001; FB-SD, W = 100, p < 0.05; FD-SB, W = 50, p < 0.01; FD, n = 9; SD, n = 8; FB, n = 16; SB, n = 6).

Figure 5: Differences in levels of synaptic drive related to speed and V2a cell type

A) Voltage-clamp (vc) recordings of excitatory post-synaptic currents (EPSCs) received by fast (top, FD) and slow (bottom, SD) V2a-D neurons along with ventral root (vr) recordings during fictive swimming triggered by an electrical stimulus (black arrowheads, artifact blanked). Black dots indicate burst intervals for frequency measures. Grey shaded boxes indicate region expanded inset, illustrating the holding potential (dashed line, -75 mV) and individual EPSCs (tick marks). Scale bars, 25 pA, 100 ms (20 ms inset).

B) As in *A*, but for fast (top, FB) and slow (bottom, SB) V2a-B neurons.

C) Scatter plot of maximum EPSC amplitude (pA) as a function of input resistance (GΩ) on logarithmic x- and y-scales. Dashed logarithmic trendlines are included for illustrative purposes (Spearman's rank correlation test, r_s = -0.873, p < 0.001, n = 39).

D) Voltage-clamp recordings of inhibitory post-synaptic currents (IPSCs) at a holding potential of 10 mV from fast (top, FD) and slow (bottom, SD) V2a-D neurons, organized as detailed in panel A. Scale bars, 100 pA, 100 ms (20 ms inset).

E) As in D, but fast (top, FB) and slow (bottom, SB) V2a-B neurons.

F) Scatter plot of maximum IPSC amplitude as a function of input resistance (GΩ) on logarithmic x- and y-scales (Spearman's rank correlation test; r_s = -0.633, p < 0.001, n = 36).

G) Top panel: Box plots of the maximum EPSC per cycle as a percentage of the maximum current (max EPSC%) for fast (FD, n = 9) and slow (SD, n = 6) V2a-D neurons, organized into 4 bins based on

1022 frequency. Dashed line indicates transition between slow carangiform and fast anguilliform modes.
1023 Bottom panel: as above, but for fast (FB, n = 11) and slow (SB, n = 5) V2a-B neurons.
1024 **H)** Top panel: Box plots of max EPSC% for fast and slow V2a-D neurons from panel G, collapsed into
1025 single slow (<35 Hz) and fast (>35 Hz) bins for purposes of statistical analysis (Wilcoxon signed-rank
1026 test; FD, V = 0, $p < 0.01$, n = 9; SD, V = 21, $p < 0.05$, n = 6). Bottom panel: As above but for V2a-B
1027 neurons (Wilcoxon signed-rank test; FB, V = 2, $p < 0.01$, n = 11; SB, V = 15, $p = 0.063$, n = 5). Boxed
1028 plots are superimposed on trendlines from individual neurons. Note, 1 cell each for V2a-D and V2a-B
1029 slow subtypes behaved more like fast subtypes (dashed lines).
1030 **I)** Top panel: Box plots of the maximum IPSC per cycle as a percentage of the maximum current (max
1031 IPSC%) for fast (FD, n = 7) and slow (SD, n = 7) V2a-Ds organized as in panel G. Bottom panel: As
1032 above but for fast (FB, n = 12) and slow (SB, n = 6) V2a-B neurons.
1033 **J)** Top panel: Box plots of max IPSC% for fast and slow V2a-D neurons from panel *I*, collapsed into single
1034 slow (<35 Hz) and fast (>35 Hz) bins for purposes of for statistical analysis (Wilcoxon signed-rank
1035 test; FD, V = 0, $p < 0.05$, n = 7; SD, V = 1, $p < 0.05$, n = 7). Bottom panel: as above, but for fast and
1036 slow V2a-B neurons (Wilcoxon signed-rank test; FB, V = 0, $p < 0.001$, n = 12; SB, V = 4, $p = 0.219$, n =
1037 6).
1038 **K)** Box plots of maximum excitatory and inhibitory current for FD (Wilcoxon signed-rank test; V = 0, p <
1039 0.01, n = 9 for excitation, n = 8 for inhibition) and SD (Wilcoxon signed-rank test; V = 0, $p < 0.05$, n =
1040 8 for excitation, n = 7 for inhibition) neurons.
1041 **L)** As in *K* but for FB (Wilcoxon signed-rank test; V = 1, $p < 0.001$, n = 16 for excitation, n = 15 for
1042 inhibition) and SB (Wilcoxon signed-rank test; V = 0, $p < 0.05$, n = 6 for excitation, n = 6 for
1043 inhibition) neurons.
1044
1045 **Figure 6: Differences in timing of synaptic drive related to speed and V2a cell type**
1046 **A)** Raw (grey) and low-pass filtered (black) traces of post-synaptic current (PSC), normalized to the peak
1047 (1) and trough (0) of phasic excitation (left) and inhibition (right). Corresponding ventral root (vr)
1048 bursts used to define in- and anti-phase (gray shaded boxes) currents are shown below. Block dots
1049 denote the peaks identified by the findpeaks() function in MATLAB. Note, excitation has been inverted
1050 to simplify comparisons to inhibition.
1051 **B)** Top panel: Circular bar plots of spike phase for fast descending (FD, n = 9) and bifurcating (FB, n = 16)
1052 V2a neurons (Watson's two-sample test of homogeneity; F = 0.483, p< 0.001). Bottom panel: Circular
1053 bar plots of spike phase for slow descending (SD, n = 8) and bifurcating (SB, n = 6) neurons (Watson's
1054 two-sample test of homogeneity; F = 3.711, p< 0.001). Scale bars, 10% total distribution.
1055 **C)** Top panel: Circular bar plots of phase normalized peaks in low pass filtered EPSCs for fast descending
1056 (FD, n = 9) and fast bifurcating (FB, n = 11) V2a neurons (Watson's two-sample test of homogeneity; F
1057 = 5.941, $p < 0.001$). Bottom panel: Circular bar plots of phase normalized peaks in low pass filtered
1058 EPSCs for slow descending (SD, n = 7) and slow bifurcating (SB, n = 6) neurons (Watson's two-sample
1059 test of homogeneity; F = 2.548, $p < 0.001$). Scale bars, 10% total distribution.

1060 **D)** Top panel: Circular bar plots of phase normalized peaks in low pass filtered IPSCs for fast descending
1061 (FD, n = 7) and fast bifurcating (FB, n = 12) neurons (Watson's two-sample test of homogeneity; F =
1062 3.646, p < 0.001). Arrowhead indicates prominent in-phase IPSC component for fast V2a-Bs. Bottom
1063 panel: Circular bar plots of phase normalized peaks in low pass filtered IPSCs for slow descending (SD,
1064 n = 7) and slow bifurcating (SB, n = 6) neurons (Watson's two-sample test of homogeneity; F = 5.426,
1065 p < 0.001). Scale bars, 10% total distribution. Arrowhead indicates prominent in-phase IPSC
1066 component for slow V2a-Ds. Scale bars, 10% total distribution.
1067 **E)** Line plots from V2a-D neurons of averaged excitation (Ex; FD, n = 9; SD, n = 6), averaged inhibition
1068 (In; FD, n = 7; SD, n = 7), and spike densities (S; FD, n = 7; SD, n = 7) broken into four ventral root
1069 burst frequency (Hz) bins. Post synaptic current was normalized on a cycle-by-cycle basis, such that
1070 the minimum and maximum current per cycle equaled 0 and 1 respectively. Scale bar for spike
1071 densities, 50% total distribution.
1072 **F)** As in panel *E*, but averaged excitation (Ex; FB, n = 11; SB, n = 5), inhibition (In; FB, n = 12; SB, n = 6),
1073 and spike densities (S; FB, n = 16; SB, n = 6) for V2a-B neurons.

1074 **Figure 7. Speed-dependent impact of silencing dI6 neurons on rhythm vs. pattern**

1075 **A)** Composite DIC/epifluorescence image of Tg[Dmrt3a:GFP] larval zebrafish at 4 days post fertilization
1076 (4d). Dorsal is up and rostral is left. Scale bar, 0.5 mm
1077 **B)** Left panel: Confocal image of the Tg[Dmrt3a:GFP] spinal cord from segments 10-12 at midbody
1078 (purple box in *A*). Scale bar, 20 µm. Right panel: Coronal view of confocal image to the left illustrating
1079 commissural axons of dI6 neurons (white arrowhead). Dashed lines indicate boundaries of spinal cord.
1080 Scale bar, 20 µm.
1081 **C)** Left panel: Composite confocal image of all dI6 somata labeled with pTagRFP (purple) and subsets of
1082 dI6 somata labeled with botulinum toxin tagged GFP (green), using a combination of compound
1083 transgenic lines (noted below). Boundaries of spinal cord are normalized to 0-1 in the dorso-ventral
1084 (DV) axis. Scale bar, 30 µm. Middle panel: Bar plots of average numbers (+/- SEM) of pTagRFP
1085 labeled dI6 neurons (purple) and BoTx-GFP labeled dI6 neurons (green) per midbody segment (n = 5-
1086 6 segments from 3 fish) along the dorso-ventral axis. The DV distributions of pTagRFP expressing (n =
1087 517) and BoTx-GFP expressing dI6 neurons (n = 842) are significantly different (Wilcoxon rank-sum
1088 test; W = 184452, p < 0.001). Right panel: Line plot of percentage of total dI6 neurons labeled with
1089 BoTx-GFP along the dorso-ventral axis. Dashed grey line indicates 50 percent of the distribution.
1090 **D)** Top panels: examples of extracellular ventral rootlet recordings recorded on the left (L) and right (R)
1091 sides in sibling control larvae lacking BoTx-GFP expression. Two consecutive swim episodes are
1092 illustrated, the first (Swim 1) is evoked by a mild electrical stimulus (s) to the tail fin (at arrowhead,
1093 artifact blanked), with subsequent episodes occurring intermittently after the first (Swim 2+). Scale
1094 bar, 500 ms. Bottom panels: examples from BoTx-GFP fish with coincident bilateral activity. Black
1095 dots illustrate ipsilateral bursts that match frequencies observed in controls. Shaded purple and green
1096 boxes illustrate left-right alternation.

1097 **E)** Left panel: Scatter plot of left-right (L-R) phase versus the time in the swim episode (s) in control
1098 siblings. Superimposed on pooled data are density plots from the swimming episode immediately
1099 following the stimulus (Swim 1) and subsequent swim episodes (Swim 2+), which are not significantly
1100 different following a Two-sample Kolmogorov-Smirnov test ($D = 0.084$, $p = 0.305$, $n = n = 330$ cycles
1101 for Swim 1 from 5 fish and 219 cycles for Swim 2+ from 4 fish). Right panel: Scatter plot of BoTxBLC-
1102 GFP fish illustrating collapse of left-right alternation and rhythmicity primarily at the beginning of
1103 the swimming episodes. In this case, density plots for Swim 1 versus Swim 2+ are significantly
1104 different (***, Two-sample Kolmogorov-Smirnov test; $D = 0.163$, $p < 0.001$, $n = 428$ cycles for Swim 1
1105 from 11 fish and 540 cycles for Swim 2+ from 10 fish).
1106 **F)** Scatter plot analyzing ventral root burstlet (vrb) frequency for control (purple) and BoTx-GFP fish
1107 (green) on the left and right sides on a cycle-by-cycle basis.
1108 **G)** Box plots of ventral rootlet burstlet frequency for control and BoTx-GFP fish during carangiform
1109 swimming below 35 Hz for Swim 1 (Wilcoxon rank-sum test; $W = 35$, $p = 0.454$, $n = 11$ BoTx-GFP and
1110 5 control fish) and Swim 2+ ($W = 26$, $p = 0.453$, $n = 10$ BoTx-GFP and 4 control fish).
1111 **H)** Box plots of ventral rootlet burstlet left-right phase for control and BoTx-GFP fish during carangiform
1112 swimming below 35 Hz for Swim 1 (Wilcoxon rank-sum test; $W = 18$, $p = 0.439$, $n = 11$ BoTx-GFP and
1113 5 control fish) and Swim 2+ ($W =17$, $p=0.733$, $n = 10$ BoTx-GFP and 4 control fish).
1114 **I)** Box plots of ventral rootlet burstlet duration for control and BoTx-GFP fish during carangiform
1115 swimming below 35 Hz for Swim 1 (Wilcoxon rank-sum test; *, $W = 48$, $p < 0.05$, $n = 11$ BoTx-GFP
1116 and 5 control fish) and Swim 2+ ($W = 27$, $p = 0.374$, $n = 10$ BoTx-GFP and 4 control fish).
1117 **J)** Box plots of ventral rootlet burstlet duty cycle for control and BoTx-GFP fish during carangiform
1118 swimming below 35 Hz for Swim 1 (Wilcoxon rank-sum test; **, $W = 52$, $p < 0.01$, $n = 11$ BoTx-GFP
1119 and 5 control fish) and Swim 2+ (*, $W = 27$, $p < 0.05$, $n = 10$ BoTx-GFP and 4 control fish).

1120 **Figure 8. Summary diagrams of cell-type-specific origins of locomotor rhythmicity**

1121 **A)** Schematic illustrating the major spinal interneuron types that provide excitation (top) and inhibition
1122 (bottom) during locomotion. Dorsal is up and rostral is left. See Discussion for details.
1123 **B)** Schematic illustrating the potential wiring diagrams between major spinal interneuron types (+,
1124 excitatory; –, inhibitory) for fast swimming (top) and slow swimming (bottom). Snapshots from high-
1125 speed videos are illustrated to the left for fast anguilliform and slow carangiform swimming. F, fast
1126 motor pools; S, slow motor pools. Dashed vertical line is midline. Reciprocal populations are shaded
1127 grey for simplicity.
1128 **C)** Schematic focusing on the major connections that differentiate fast and slow swimming circuits.
1129 Rhythm-generating circuitry is in blue and pattern-forming circuitry is in black.
1130

1131 **Video 1. High-speed video of real escape swimming in a 5 day old larva**

1132 A) Larva is touched near the head by a sharpened tungsten pin, which triggers a rapid escape bend,
1133 followed by high-frequency anguilliform swimming and then ending with low-frequency carangiform

swimming. Video was captured at 2000 frames per second and has been slowed down 40X for purposes of visualization (playback at 50 frames per second).

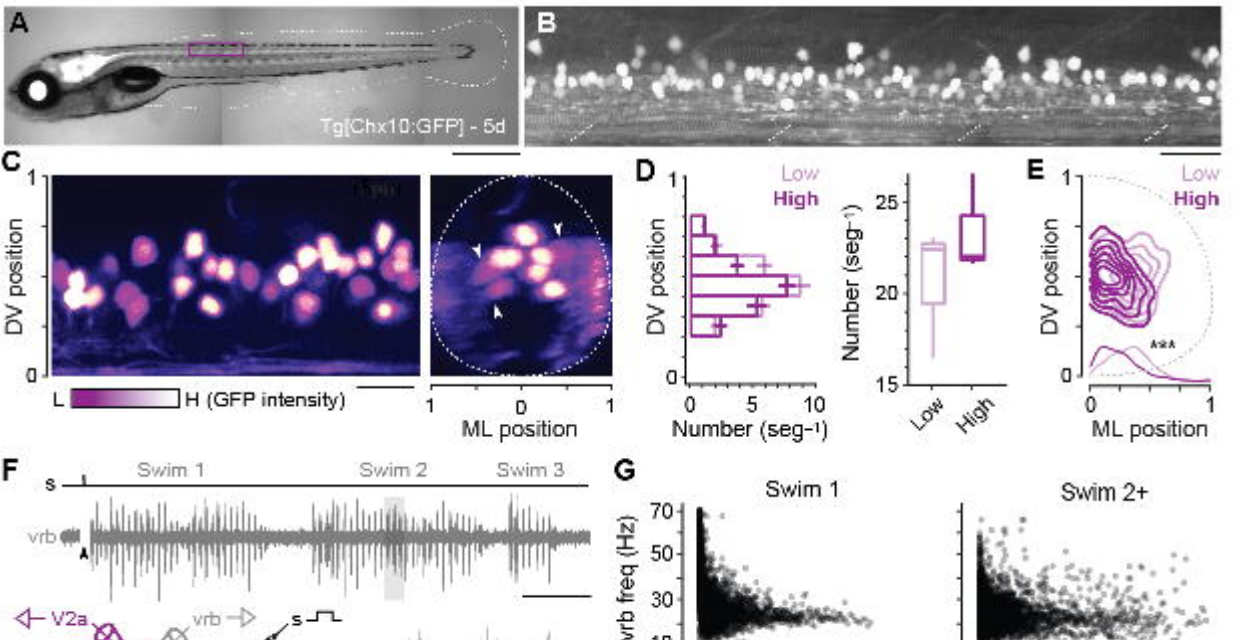
A
Tg[Chx10:GFP] - 5d
B
C
DV position
L
H (GFP intensity)
ML position
D
Low
High
DV position
Number (seg⁻¹)
Number (seg⁻¹)
Low
High
E
Low
High
DV position
ML position
F
Swim 1
Swim 2
Swim 3
s
vrb
V2a
vrb
s
G
Swim 1
Swim 2+
vrb freq (Hz)
Time in swim (s)
Time in swim (s)

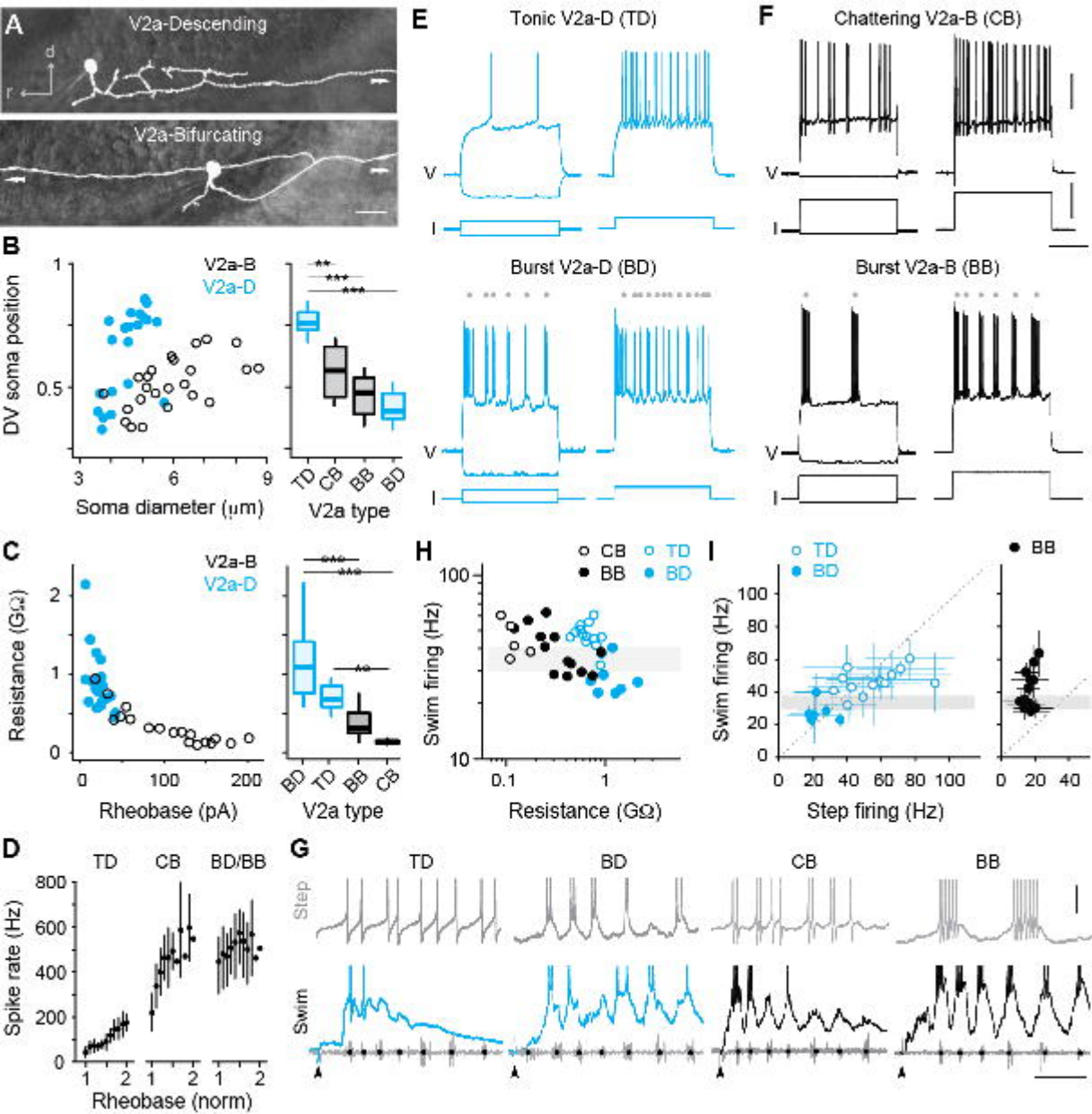
A
V2a-Descending
d
r
V2a-Bifurcating
B
V2a-B
V2a-D
DV soma position
Soma diameter (μm)
V2a type
TD
CB
BB
BD
C
Resistance (GΩ)
Rheobase (pA)
D
TD
CB
BD/BB
Spike rate (Hz)
Rheobase (norm)
E
Tonic V2a-D (TD)
Burst V2a-D (BD)
F
Chattering V2a-B (CB)
Burst V2a-B (BB)
V
I
G
Step
Swim
H
Swim firing (Hz)
Resistance (GΩ)
I
Step firing (Hz)

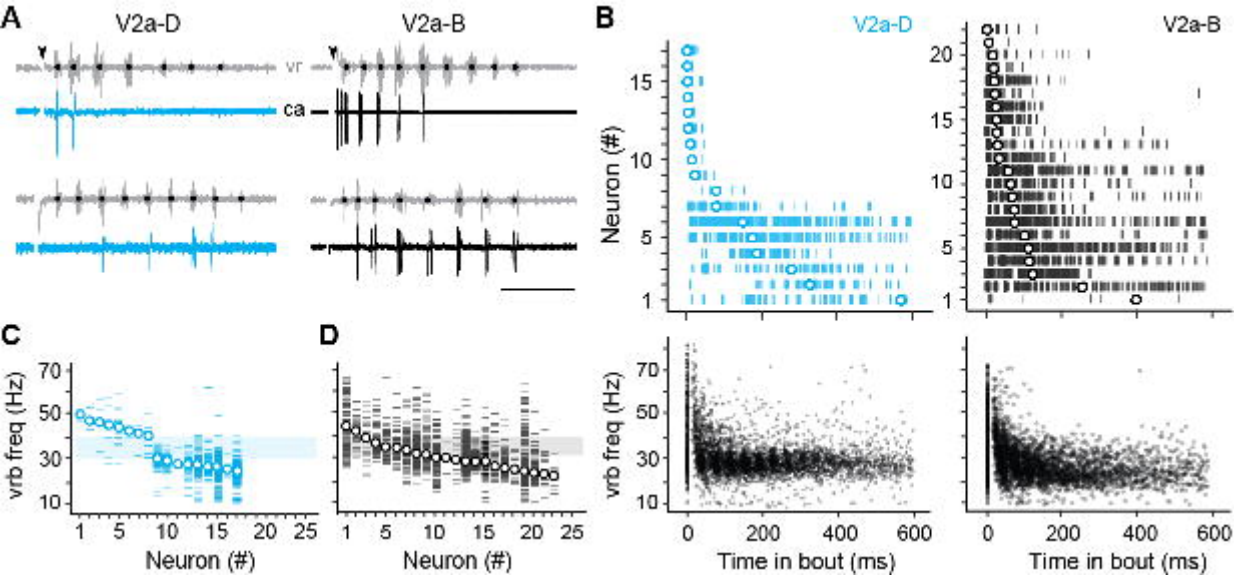
A
V2a-D
V2a-B
vr
ca
B
V2a-D
V2a-B
Neuron (#)
C
D
vrb freq (Hz)
Neuron (#)
Time in bout (ms)

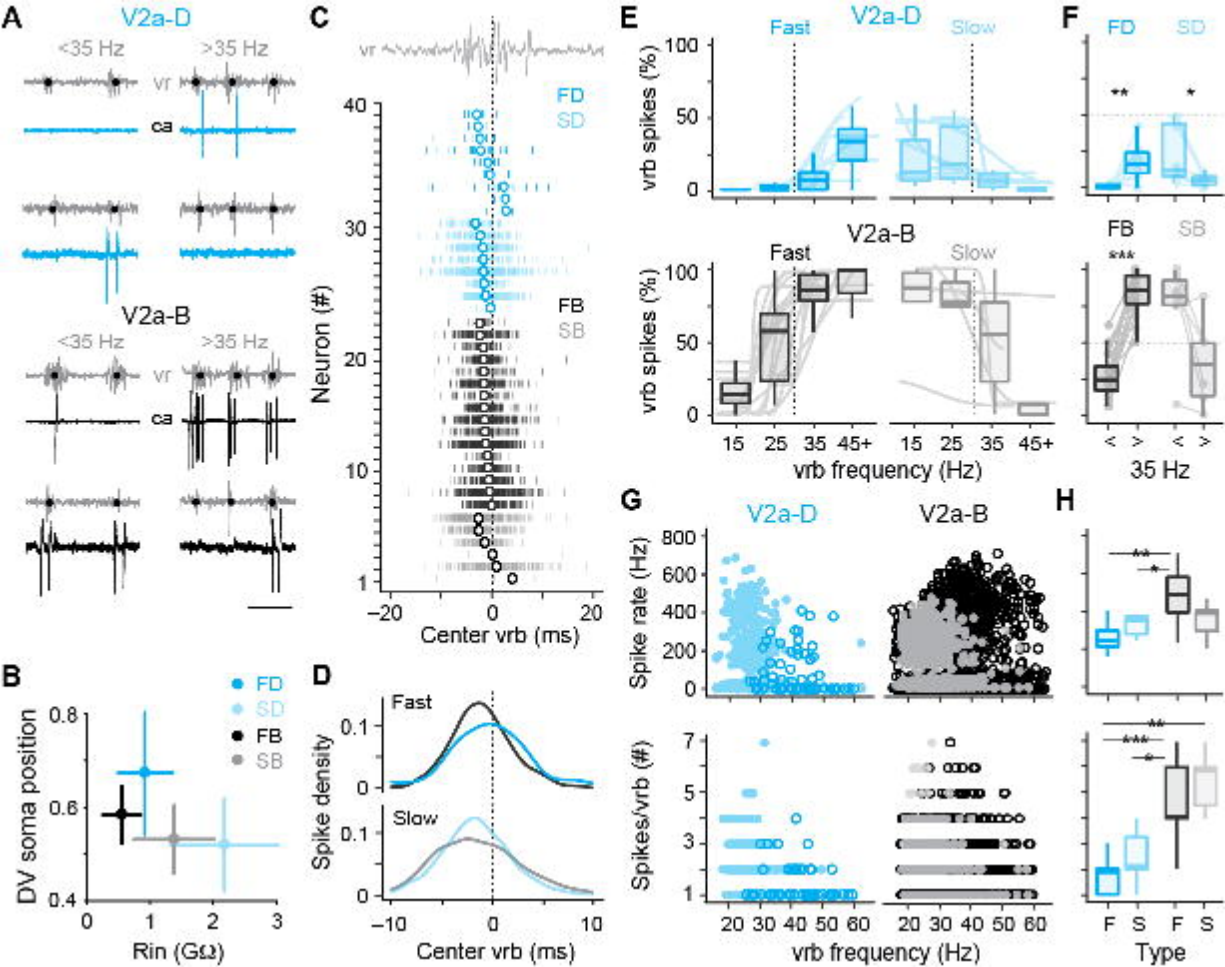
A
V2a-D
<35 Hz
>35 Hz
vr
ca
V2a-B
<35 Hz
>35 Hz
vr
ca
B
FD
SD
FB
SB
DV soma position
Rin (GΩ)
C
vr
FD
SD
FB
SB
Neuron (#)
Center vrb (ms)
D
Fast
Slow
Spike density
Center vrb (ms)
E
Fast
V2a-D
Slow
vrb spikes (%)
V2a-B
Fast
Slow
vrb spikes (%)
vrb frequency (Hz)
F
FD
SD
FB
SB
35 Hz
G
V2a-D
V2a-B
Spike rate (Hz)
Spikes/vrb (#)
vrb frequency (Hz)
H
Type

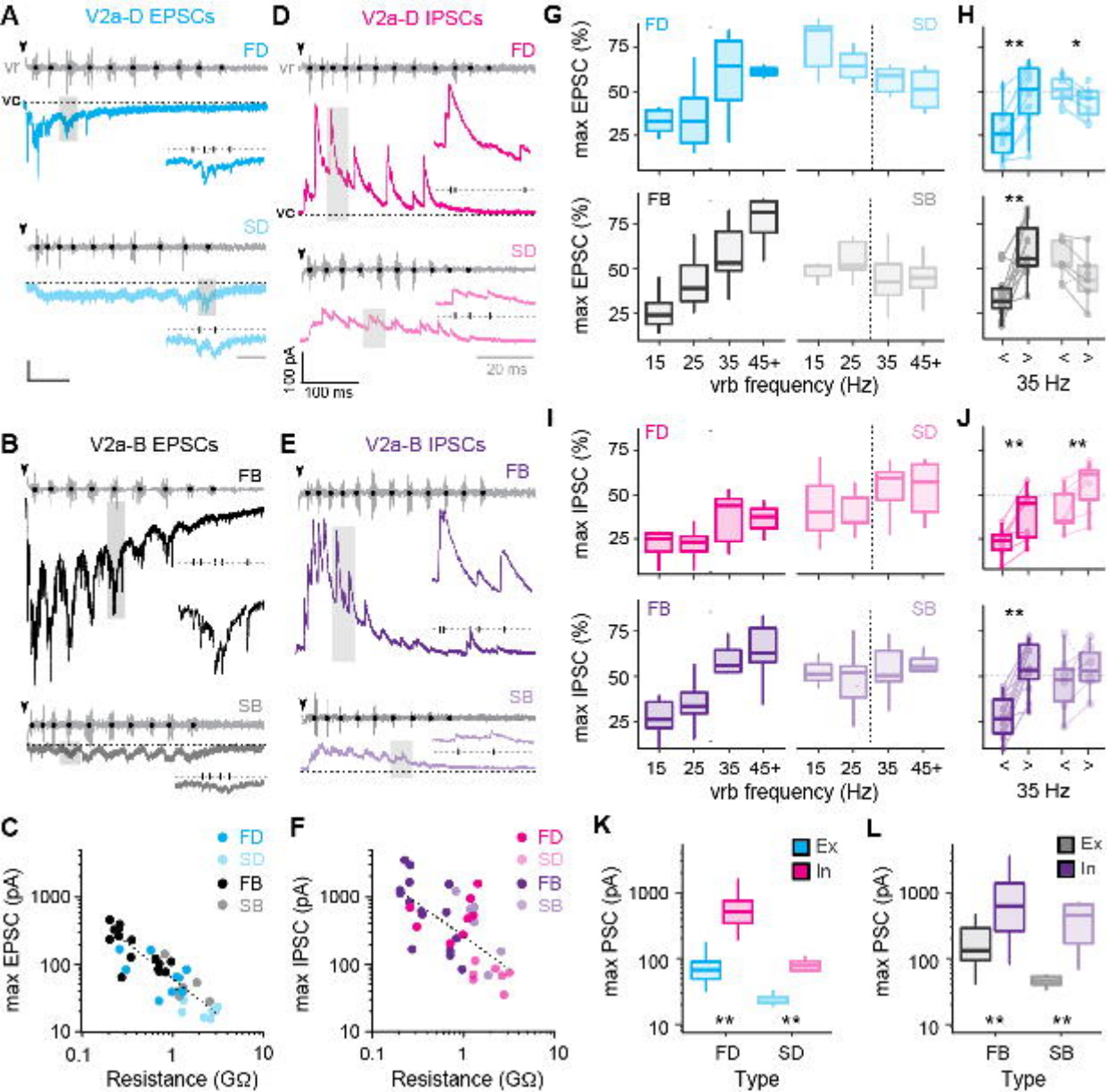
A
V2a-D EPSCs
FD
vr
vc
SD
D
V2a-D IPSCs
FD
vr
vc
SD
100 pA
100 ms
20 ms
B
V2a-B EPSCs
FB
SB
E
V2a-B IPSCs
FB
SB
G
FD
SD
FB
SB
max EPSC (%)
75
50
25
15
25
35
45+
vrb frequency (Hz)
H
**
*
**
< >
35 Hz
I
FD
SD
FB
SB
max IPSC (%)
vrb frequency (Hz)
J
**
**
**
C
FD
SD
FB
SB
max EPSC (pA)
1000
100
10
0.1
1
10
Resistance (GΩ)
F
max IPSC (pA)
Resistance (GΩ)
K
Ex
In
max PSC (pA)
**
**
FD
SD
Type
L
Ex
In
max PSC (pA)
**
**
FB
SB
Type

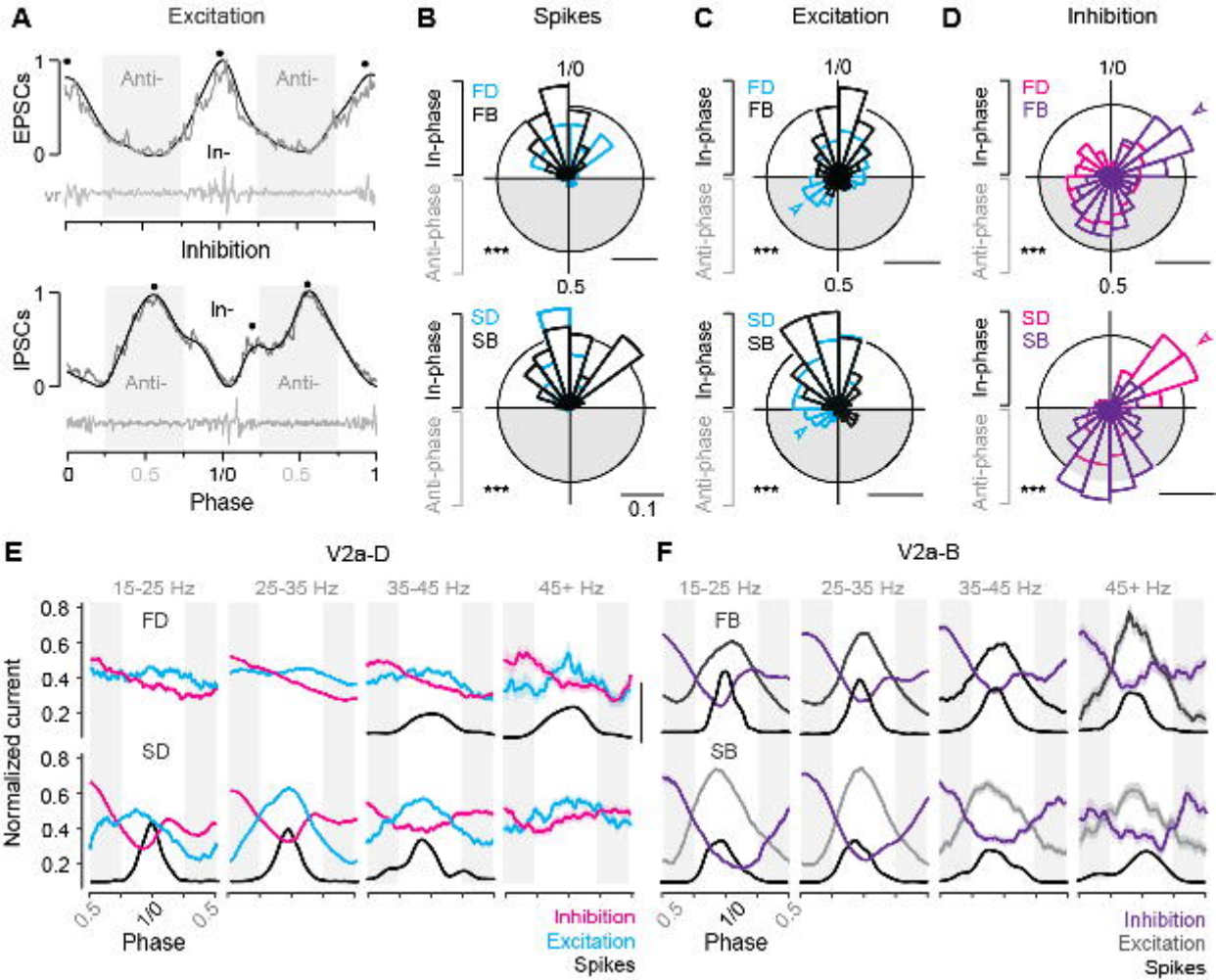
A
Excitation
EPSCs
Anti-
Anti-
In-
vr
Inhibition
IPSCs
In-
Anti-
Anti-
0
0.5
1/0
0.5
1
Phase
B
Spikes
C
Excitation
D
Inhibition
1/0
0.5
FD
FB
SD
SB
In-phase
Anti-phase
***
0.1
E
V2a-D
F
V2a-B
15-25 Hz
25-35 Hz
35-45 Hz
45+ Hz
Normalized current
0.8
0.6
0.4
0.2
Phase
Inhibition
Excitation
Spikes

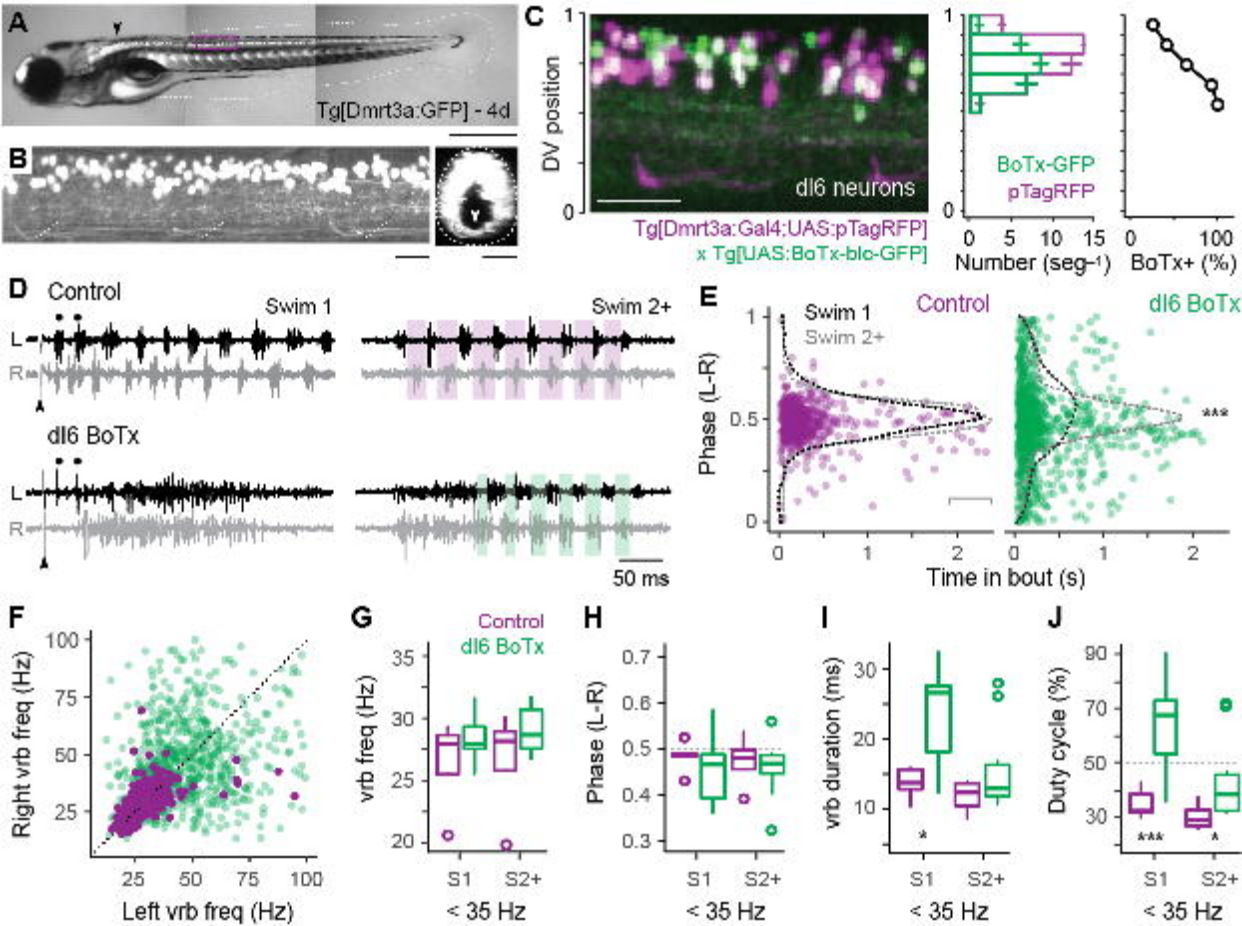
A
Tg[Dmrt3a:GFP] - 4d
B
C
DV position
dI6 neurons
Tg[Dmrt3a:Gal4;UAS:pTagRFP]
x Tg[UAS:BoTx-blc-GFP]
BoTx-GFP
pTagRFP
Number (seg⁻¹)
BoTx+ (%)
D
Control
Swim 1
Swim 2+
dI6 BoTx
L
R
50 ms
E
Swim 1
Swim 2+
Control
dI6 BoTx
Phase (L-R)
Time in bout (s)
***
F
Right vrb freq (Hz)
Left vrb freq (Hz)
G
Control
dI6 BoTx
vrb freq (Hz)
S1
S2+
< 35 Hz
H
Phase (L-R)
I
vrb duration (ms)
J
Duty cycle (%)

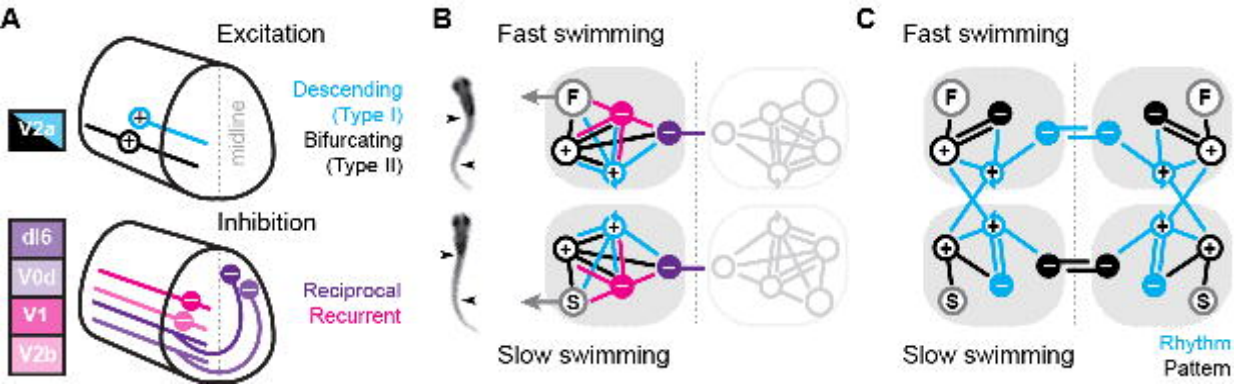
A
Excitation
V2a
midline
Descending
(Type I)
Bifurcating
(Type II)
Inhibition
dI6
V0d
V1
V2b
Reciprocal
Recurrent
B
Fast swimming
F
S
Slow swimming
C
Fast swimming
F
F
S
S
Slow swimming
Rhythm
Pattern